International Journal of Heat and Mass Transfer 208 (2023) 124049

Contents lists available at ScienceDirect

International Journal of Heat and Mass Transfer

journal homepage: www.elsevier.com/locate/hmt

Thermocapillary convection in superimposed layers of self-rewetting fluids: Analytical and lattice Boltzmann computational study

Bashir Elbousefi, William Schupbach, Kannan N. Premnath*, Samuel W.J. Welch

Department of Mechanical Engineering, University of Colorado Denver, 1200 Larimer Street, Denver, CO 80204, USA

ARTICLE INFO

Article history:
Received 11 October 2022
Revised 26 February 2023
Accepted 1 March 2023
Available online 13 March 2023

Keywords:
Thermocapilly convection
Self-rewetting fluids
Microchannels
Lattice Boltzmann method
Central moments
Multiphase Flow
Analytical solution

ABSTRACT

Self-rewetting fluids (SRFs), such as aqueous solutions of long-chain alcohols, exhibit anomalous quadratic dependence of surface tension on temperature having a minimum and with a positive gradient. When compared to the normal fluids (NFs) that have negative gradient of surface tension on temperature, the SRFs can be associated with significantly modified interfacial dynamics, which have recently been exploited to enhance flow and thermal transport in various applications. In this work, first, we develop a new analytical solution of thermocapillary convection in superimposed two SRF layers confined within a microchannel that is sinusoidally heated on one side and maintained at a uniform temperature on the other side. Then, a robust central moment lattice Boltzmann method using a phase-field model involving the Allen-Cahn equation for interface tracking, two-fluid motion, and the energy transport for numerical simulations of SRFs is constructed. The analytical and computational techniques are generally shown to be in good quantitative agreement with one another. Moreover, the effect of the various characteristic parameters on the magnitude and the distribution thermocapillary-driven motion is studied. The thermocapillary flow patterns in SRFs are shown to be strikingly different when compared to the NFs: For otherwise the same conditions, the SRFs result in eight periodic counterrotating thermocapillary convection rolls, while the NFs exhibit only four such vortices. Moreover, the direction of the circulating fluid motion in such vortical structures for the SRFs is found to be towards the hotter zones on the interfaces, which is opposite to that in NFs. These features are found to be sustained even as the interfaces deforms in simulations. By tuning the sensitivity coefficients of the surface tension on temperature, it is shown that not only the magnitude of the thermocapillary velocity can be significantly manipulated, but also the overall flow patterns as well. It is also demonstrated that the thermocapillary convection can be enhanced if the SRF layer adjacent to the nonuniformly heated wall is made relatively thinner or has higher thermal conductivity ratio or has smaller viscosity when compared to that of the other fluid layer. The peak Marangoni velocity is found to be increased by a factor of 2 by doubling the dimensionless quadratic surface tension sensitivity coefficient and by about an order of magnitude as the fluid thickness ratio is changed from 1/3 to 3.

1. Introduction

Surface tension forces arising at the interface between fluids play prominent role in many multiphase and thermal transport processes [1]. Their variations can be caused by changes in the local interfacial temperature or with the addition of surface active materials (i.e., surfactants). The surface tension gradients result in the so-called Marangoni stresses [2], which, via the viscous effects of the fluids, induce their convective motions in the vicinity of the interfaces [3]. If they are set up due to local temperature variations, they are referred to as the thermocapillary convection. Since the seminal study by Young et al. [4], who demonstrated the ability of a bubble to migrate towards hot regions in the absence of gravity due to Marangoni stresses, thermocapillary effects have been exploited in controlling the motion of dispersed phases (bubbles or drops) in fluids, especially in microgravity applications [5] (see e.g., Welch [6], Ma and Bothe [7] for related numerical investigations). On the other hand, in micro-electro-mechanical-systems, as the scales of the devices are reduced, the interfacial forces dominate, and the thermocapillary convection can be utilized to manipulate the motion of fluid streams and thermal transport phenomena in microchannels (see e.g., Darhuber and Troian [8], Karbalaei et al. [9], Pendse and Esmaeeli [10], Gambaryan-Roisman [11]).

Common fluids have the property of surface tension that decreases somewhat linearly with increasing temperatures. On the

---

* Corresponding author.
E-mail address: kannan.premnath@ucdenver.edu (K.N. Premnath).

https://doi.org/10.1016/j.ijheatmasstransfer.2023.124049
0017-9310/© 2023 Elsevier Ltd. All rights reserved.

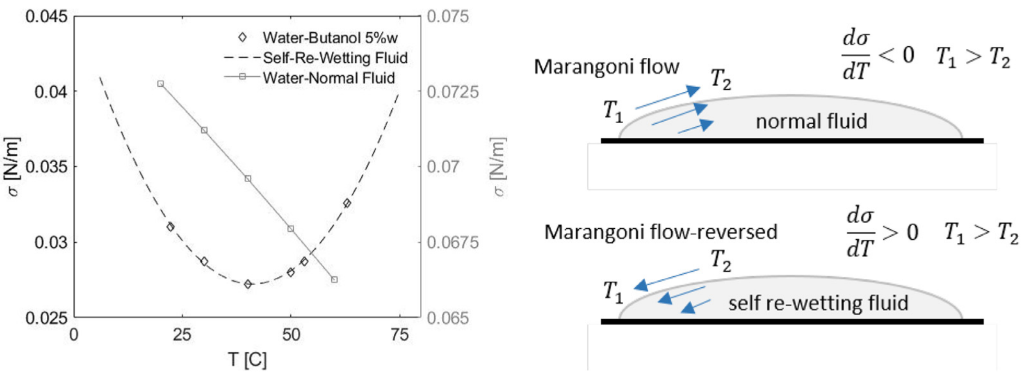

(a) (b)

Fig. 1. (a) Surface tension variation with respect to temperature for a normal fluid (NF) and for a self-rewetting fluid (SRF). The parabolic variation of the surface tension for the example SRF with temperature is based on a curve fit of the data given in Savino et al. [18]. (b) Differences in the thermocapillary motions in the vicinity of interfaces for NFs and SRFs.

other hand, certain fluids, such as aqueous solutions of long-chain (i.e., “fatty”) alcohols, some liquid metallic alloys, and nematic liquid crystals exhibit anomalous nonlinear parabolic dependence of surface tension on temperature with a range involving its positive gradient. In particular, Vochten and Petre [12] performed measurements in non-azeotropic, high-carbon alcohol solutions (such as n-butanol), and demonstrated that beyond a certain threshold temperature, their surface tension will increase with further increase in temperature; the surface tension becomes a minimum at this threshold temperature, whose value increases for alcohols with longer carbon chains; and for a particular alcohol, the minimum surface tension decreases monotonically with its concentration. These findings were corroborated by follow on experimental studies reported in Petre and Azouni [13], Limbourg-Fontaine et al. [14], Villers and Platten [15], and such fluids have been named as “self-rewetting” fluids (SRFs) by Abe et al. [16] due to a significantly altered thermocapillary convection promoting a desired wetting effect when compared to the common or normal fluids (NFs). In particular, the Marangoni stresses induce the motion of fluids in the vicinity of the interfaces towards higher temperatures in SRFs, which is opposite to that observed in NFs (see Fig. 1). As such, the self-rewetting fluids have the ability to generate vigorous inflow of liquids near high temperature regions, e.g., towards nucleating sites during boiling thereby preventing the onset of dry patches at such hot spots. These and other peculiar features of SRFs have provided strong impetus for their investigations as novel classes of fluids to enhance transport in various thermal management applications during the last two decades. They have been proposed as working fluids in various applications in both terrestrial and microgravity environments [16,17]. The use of SRFs has been shown to improve heat transfer efficiency in heat pipes [18–23], flow boiling [24] and evaporation [25] in microchannels, pool boiling processes [26–29], and two-phase heat transfer devices using self-rewetting gold nanofluids [30]. Moreover, the peculiar characteristics of the migration of bubbles in SRFs have been experimentally studied in Shanahan and Sefiane [31], Mamalis et al. [32].

As noted in a recent review involving the use of SRFs [33], only limited analytical and numerical studies involving the SRFs, which can provide fundamental insights into the details of the transport phenomena, have been performed. Analytical investigations into the behavior of thin films of SRFs were presented in Oron and Rosenau [34], Batson et al. [35], Yu [36] and a similarity solution of the motion of SRFs in an unbounded domain was discussed in Slavtchev and Miladinova [37]. Theoretical analysis of the migration of a bubble in a SRF was presented in Tripathi et al. [38] and that of an elongated slug in Duffy et al. [39]. More recently, numerical studies on the migration of a bubble in SRFs were performed in Balla et al. [40], Majidi et al. [41], Mitchell et al. [42]. Among the various computational methods, the lattice Boltzmann (LB) method, a technique inspired from kinetic theory [43–45], has shown promising capabilities for simulating multiphase flows (see e.g., He et al. [46], He and Doolen [47], Lee and Lin [48], Premnath and Abraham [49], Hajabdollahi et al. [50]). The LB methods have also been applied to simulate thermocapillary flow problems (see e.g., Majidi et al. [41], Mitchell et al. [42], Liu et al. [51]). More recently, using robust collision models [52], the LB method has been extended to simulate multiphase flows at high density ratios and including Marangoni stresses [50], which will serve as a basis for further extension for its application to an interesting configuration involving thermocapillary flows in SRFs as discussed below.

One of the important applications of exploiting thermocapillarity is in manipulating the motion of continuous streams of fluids confined within microchannels. In this regard, in the case of two superimposed normal fluids (NFs), Pendse and Esmaeeli [10] presented a theoretical analysis for thermocapillary convection driven by periodic heating from the bounding walls, representing, for example, micropatterned walls.

In this work, we generalize the above mentioned configuration reported in Ref. [10] and develop a new analytical solution for thermocapillary convection in two superimposed layers of self-rewetting fluids (SRFs) confined within a microchannel and subjected to periodic heating on the lateral walls. Such an investigation yields a new pathway to enhance mixing and transport by tuning thermocapillary effects in SRFs when compared to NFs in differentially heated microchannels. We derive analytical solutions for the thermocapillary convection currents in SRFs under the assumptions of small capillary and Marangoni numbers and in the creeping flow limit, which are representative of situations in microchannels. The solution will be parameterized by the thickness ratio of the fluids and the ratios of the thermal conductivities as well as that of viscosities, and the coefficients of the functional dependence of surface tension on temperature. As a second objective, we will also present a numerical simulation approach based on a robust central moment LB scheme using a phase field model based on the conservative Allen–Cahn equation by extending and improving our recent work [50]. It involves computing the evolution of three distribution functions, one each for the flow field, temperature field and the capturing of the interfaces via a order parameter, and with an attendant surface tension equation of state for SRFs. As a third objective, we will compare the predictions based on our analytical solution against the results from our LB computational

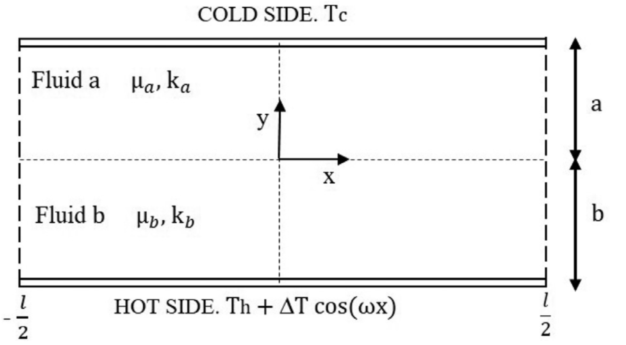

Fig. 2. Schematic of the geometric setup for two superimposed self-rewetting fluid (SRF) layers within a horizontal microchannel with a periodic heating at the bottom wall.

approach, thereby demonstrating qualitative as well as quantitative consistency between the two approaches, and thus establishing the validity of our analysis. Finally, we aim to present a study of the effect of the various characteristic parameters on the vortical convection patterns in SRFs, in terms of both the number of convection cells and their sense of direction of motion and comparing and contrasting them with that of NFs, and on the magnitude of the thermal convection velocities. These contributions not only serve in elucidating the physics in a fundamental configuration, but the analytical solutions developed herein could also serve as a benchmark for any new computational techniques for simulating thermocapillary flows in SRFs in future. Moreover, the numerical algorithm based on the LB method presented in this work, while applied here in what follows for SRF layers in a microchannel, can also be readily extended for other situations including those involving tracking the motion of any dispersed phase in SRFs.

This paper is organized as follows. In the next section (Section 2), we will discuss the problem setup of the thermocapillary flow in superimposed layers of SRFs in a microchannel and the attendant governing equations for incompressible two-fluid motion, energy transport and the interfacial equation of state. The new analytical solution is derived in Section 3. The computational model equations for the LB schemes for multiphase flows using a phase field model are given in Section 4. The discretized central moment LB algorithms for simulating multiphase flows of SRFs are summarized in various subsections of the Appendix A with additional supporting details in Appendix B. Section 5 presents a numerical validation of the computational approach. The results and discussion of the effect of various characteristic parameters are presented in Section 6; moreover, the utility of the computational method in simulating such flows with interfacial deformations at higher capillary numbers is also demonstrated. The main findings and contributions of this work are summarized in Section 7.

2. Problem setup, governing equations, and interface equation of state

2.1. Problem setup

A schematic of the geometric configuration of two superimposed SRF layers confined within a microchannel is shown in Fig. 2. The channel is of horizontal length l and whose walls are separated by a lateral distance $(a+b)$. A sinusoidal temperature variation is imposed on the hot bottom wall side, while cold bottom wall side is maintained at a uniform temperature. The channel is filled with two immiscible SRFs, fluid ‘a’ on the top side and fluid ‘b’ on the bottom side with thicknesses a and b, respectively; the viscosities and thermal conductivities of the top fluid are denoted by μ_a and k_a, respectively, while those for the bottom fluid are represented by μ_b and k_b, respectively. The upper wall is set with a constant reference cold temperature T_c, while the lower wall is prescribed with a spatially varying hot temperature based on a sinusoidal profile involving a reference temperature T_h and a peak amplitude ΔT for the variation. Thus, the boundary conditions at these two sides can be written as

$$T^a(x, a) = T_c, \tag{1}$$

and

$$T^b(x, -b) = T_h + \Delta T\cos(\omega x), \tag{2}$$

where $\omega = 2\pi/l$ is the wavenumber based on the channel length l, and assume $T^b(x, -b) \geq T^a(x, a)$ for any x and $\Delta T > 0$. Here, and in what follows, we use a superscript notation with ‘a’ or ‘b’ to label any quantity associated with a top or bottom fluid, respectively. Heat diffusion into the bulk regions of the fluids then sets up a nonuniform distribution of the temperature along the interface. The surface tension $\sigma = \sigma(T)$ at the interface between the SRFs also then varies locally, which, via the viscous actions in the bulk fluids, induce a thermocapillary convection. The resulting flow field is then subject to the no-slip condition for the velocity components at the bounding walls.

2.2. Bulk fluid motion and energy transport

The thermocapillary convection in the SRFs obey the equations of mass and momentum (i.e., Navier-Stokes equations (NSE)) and the energy transport. They can be respectively written as follows:

$$\nabla\cdot\boldsymbol{u} = 0, \tag{3a}$$

$$\rho\left(\frac{\partial\boldsymbol{u}}{\partial t} + \nabla\cdot(\boldsymbol{u}\boldsymbol{u})\right) = -\nabla p + \nabla\cdot\left[\mu(\nabla\boldsymbol{u} + \nabla\boldsymbol{u}^{\dagger})\right], \tag{3b}$$

$$\frac{\partial T}{\partial t} + \boldsymbol{u}\cdot\nabla T = \nabla\cdot\left(\alpha\nabla T\right), \tag{3c}$$

where ρ, μ and α are the fluid density, dynamic viscosity, and thermal diffusivity of the fluid, respectively, with $\alpha = k/(\rho c_p)$ based on the thermal conductivity k and specific heat c_p. In the above, $\boldsymbol{u}$, p, and T denote the velocity, pressure, and temperature fields of the fluids, respectively, and the superscript symbol † represents taking transpose.

2.3. Interface equation of state for surface tension

At the interface, we need to impose an equation for the surface tension relating it to the variations in the local temperature. For the SRF, we consider the following nonlinear (parabolic) dependence of surface tension on temperature:

$$\sigma(T) = \sigma_0 + \sigma_T(T - T_{ref}) + \sigma_{TT}(T - T_{ref})^2, \tag{4}$$

where σ_0 denotes the value of the surface tension at a reference temperature T_{ref}, $\sigma_T = \frac{d\sigma}{dT}\Big|_{T_{ref}}$ and $\sigma_{TT} = \frac{1}{2}\frac{d^2\sigma}{dT^2}\Big|_{T_{ref}}$ are the coefficients of the surface equation of state, expressing the sensitivity of the surface tension on temperature. It should be noted that for a SRF, $\sigma_{TT} \neq 0$, while for a NF, $\sigma_{TT} = 0$ where only σ_T is non-zero. In general, σ_0, T_{ref}, σ_T, and σ_{TT} are properties, which are unique to a chosen SRF. In addition, at the interface, a relation between the Marangoni stress due to the nonuniform tangential surface tension gradient and the viscous fluid stress, along with the interfacial continuity conditions need to be imposed. These will be accounted for in what follows.

When the above governing equations are nondimensionalized using a reference velocity scale U and a length scale b corresponding to the thickness of the bottom SRF layer, we obtain the following dimensionless groups: Reynolds number Re, Marangoni number Ma, and the capillary number Ca, which can be defined as

$$\mathrm{Re} = \frac{Ub}{\nu_b}, \qquad \mathrm{Ma} = \frac{Ub}{\alpha_b} = \mathrm{RePr}, \quad \text{and} \quad \mathrm{Ca} = \frac{U\mu_b}{\sigma_0}. \tag{5}$$

respectively. Here, $\nu = \mu/\rho$ is the kinematic viscosity, and Pr is the Prandtl number ($\mathrm{Pr} = \nu/\alpha$). In addition, the thermocapillary convection in SRFs is governed by the following ratios of the bulk material properties

$$\tilde{\rho} = \frac{\rho_a}{\rho_b}, \qquad \tilde{\mu} = \frac{\mu_a}{\mu_b}, \qquad \tilde{k} = \frac{k_a}{k_b}, \quad \text{and} \quad \tilde{c}_p = \frac{c_{p_a}}{c_{p_b}}, \tag{6}$$

and the dimensionless parameters for the interface equation of state for the surface tension

$$M_1 = \sigma_T\left(\frac{\Delta T}{\sigma_0}\right), \quad M_2 = \sigma_{TT}\left(\frac{\Delta T^2}{\sigma_0}\right). \tag{7}$$

As in the above, taking reference values for the properties using those for the bottom fluid, by balancing the scale for the viscous shear stress $\mu_b U/b$ with that of the Marangoni stress due to the surface tension gradient $|d\sigma/dT|(\Delta T/l)$, we can estimate the scale for the reference velocity U of thermocapillary convection used in the above via $U \sim |d\sigma/dT|(\Delta T/\mu_b)(b/l)$, where ΔT is set to be equal to the maximum amplitude in the spatial variation in the imposed temperature at the bottom wall T_0, and $|d\sigma/dT|$ follows from Eq. (4).

3. Analytical solution for thermocapillary convection in superimposed SRF layers in a microchannel

We will now derive a new analytical solution for thermocapillary convection in superimposed SRF layers in the Stokes flow regime relevant to microchannels. In this regard, we consider the fluids to be incompressible, immiscible, and Newtonian, and assume that the Reynolds and Marangoni numbers are much less than one (i.e., $\mathrm{Re} \ll 1$ and $\mathrm{Ma} \ll 1$), so that the convective transport of momentum and energy can be neglected. Also, the capillary number is also taken to be much less than one (i.e., $\mathrm{Ca} \ll 1$), so that we can consider the interface to be nearly flat, and the established thermocapillary convection patterns are steady. Based on these considerations, all the conservation equations given above simplify considerably. The mass conservation read as

$$\nabla \cdot \boldsymbol{u} = 0, \tag{8}$$

while the momentum equation now reduces to

$$-\nabla p + \mu \nabla^2 \boldsymbol{u} = 0, \tag{9}$$

and the balance of thermal energy equation is given as

$$\nabla^2 T = 0, \tag{10}$$

where $\nabla^2 = \frac{\partial^2}{\partial x^2} + \frac{\partial^2}{\partial y^2}$. These bulk transport equations need to be solved in conjunction with the interface continuity conditions for the flow and temperature fields and the Marangoni stress condition at the interface between the SRFs (see below for details).

3.1. Temperature field

The thermal energy equation Eq. (10), which satisfies the wall boundary conditions given in the previous section, can be solved readily and is independent of the nature of the fluid; the specific details are given in Appendix C of this paper. The solution for the temperature field is summarized here as follows: In the upper fluid a,

$$\begin{aligned} T^a(x,y) = {} & \frac{(T_c - T_h)y + T_c\tilde{k}b + T_h a}{(a + b\tilde{k})} \\ & + \Delta T f(\tilde{a},\tilde{b},\tilde{k}) \sinh(\tilde{a} - \omega y)\cos(\omega x), \end{aligned} \tag{11}$$

and in the lower fluid b,

$$\begin{aligned} T^b(x,y) = {} & \frac{\tilde{k}(T_c - T_h)y + T_c\tilde{k}b + T_h a}{(a + b\tilde{k})} \\ & + \Delta T f(\tilde{a},\tilde{b},\tilde{k})[\sinh(\tilde{a})\cosh(\omega y) \\ & - \tilde{k}\sinh(\omega y)\cosh(\tilde{a})\big]\cos(\omega x), \end{aligned} \tag{12}$$

where $\tilde{k} = k_a/k_b$, $\tilde{a} = a\omega$, and $\tilde{b} = b\omega$ are the dimensionless parameters, and the expression for the function $f(\tilde{a},\tilde{b},\tilde{k})$ is given in Eq. (61) in Appendix C.

3.2. Flow field: stream function

Next, for obtaining the flow field driven by thermocapillary effects in SRFs, for convenience, we introduce the stream function ψ defined based on the components of the velocity field $\boldsymbol{u} = (u, v)$ as

$$u = -\frac{\partial\psi}{\partial y}, \quad \text{and} \quad v = -\frac{\partial\psi}{\partial x}, \tag{13}$$

so that the continuity equation Eq. (8) is satisfied automatically, and the momentum equation (Eq. (9)) can be entirely rewritten in terms of a single scalar variable ψ. For the latter purpose, taking the of 'curl' Eq. (9) and using $\nabla \times \nabla p = 0$ and invoking Eq. (13), we finally obtain the following biharmonic equation for the stream function [53]:

$$\nabla^4\psi = \nabla^2(\nabla^2\psi) = 0. \tag{14}$$

Since Eq. (14) is linear, we can apply the method of separation of variables by assuming the solution of ψ to be product of two solutions $X(x)$ and $Y(x)$ as

$$\psi(x,y) = X(x)Y(y).$$

Since the thermocapillary flow is established by the tangential stress at the interface, we can establish the form of the solution $X(x)$ by considering the Marangoni interfacial condition reflecting a balance between the viscous shear stress and the surface tension gradient given by

$$\left(\tau^b_{xy} - \tau^a_{xy}\right)\bigg|_{y=0} = \frac{d\sigma}{dT}\frac{\partial T}{\partial x}\bigg|_{y=0}, \tag{15}$$

where $\tau_{xy} = \mu\left(\frac{\partial u}{\partial y} + \frac{\partial v}{\partial x}\right)$ is the viscous shear stress and $d\sigma/dT$ for SRFs follows from Eq. (4) as

$$\frac{d\sigma}{dT} = \sigma_T + 2\sigma_{TT}\left(T - T_{ref}\right) = \left(\sigma_T - 2\sigma_{TT}T_{ref}\right) + 2\sigma_{TT}T.$$

Now, from Eq. (11), it follows that $\frac{\partial T}{\partial x}\big|_{y=0} \sim \sin(\omega x)$ and from the last equation together with using Eq. (11) for $T(x, y = 0)$, we have $d\sigma/dT \sim \cos(\omega x)$. Using these two estimates for the horizontal spatial variations in Eq. (15), it can be readily inferred that $\tau_{xy} \sim \alpha_1\sin(\omega x) + \alpha_2\sin(\omega x)\cos(\omega x)$, where α_1 and α_2 are some lumped constants; this suggests that the stream function to be split into a linear combination of two distinct product solutions with known spatial distribution in the x direction as in

$$\psi(x,y) = f(y)\sin(\omega x) + g(y)\sin(\omega x)\cos(\omega x), \tag{16}$$

where $f(y)$ and $g(y)$ are the two unknown functions, which will to be determined in what follows. Here, it should be noted that the first term in the last equation (Eq. (16)), $f(y)\sin(\omega x)$ arises from the linear part of the surface tension equation of state (which recovers the special case of the NFs given in Pendse and Esmaeeli [10]), while the second term $g(y)\cos(\omega x)\sin(\omega x)$ emerges from including the quadratic term for $\sigma(T)$ to encompass the more general SRFs.

Substituting Eq. (16) in Eq. (14) and simplifying results in the following two 4th order differential equations for the unknown functions $f(y)$ and $g(y)$:

$$f'''' - 2\omega^2 f'' + \omega^4 f = 0, \tag{17a}$$

$$g'''' - 8\omega^2 g'' + 16\omega^4 g = 0. \tag{17b}$$

Equation (17a) has solutions of the form $f(y) = e^{my}$, where m is a constant to be determined from the characteristic equation $(m^2 - \omega^2)^2 = 0$, giving $m = \pm\omega$. The four solutions of $f(y)$ are $e^{\omega y}$, $ye^{\omega y}$, $e^{-\omega y}$, and $ye^{-\omega y}$ because it has double roots. Similarly, for Eq. (17b), the solutions are of the form $g(y) = e^{ny}$, with the characteristic equation $(n^2 - 4\omega^2)^2 = 0$, yielding the four possible solutions of $g(y)$ as $e^{2\omega y}$, $ye^{2\omega y}$, $e^{-2\omega y}$, and $ye^{-2\omega y}$. Because the vertical direction is finite, it is convenient to employ hyperbolic functions in lieu of the exponential functions. As a result, the general form of the stream function $\psi(x, y)$ for the upper fluid can be written as

$$\begin{aligned}\psi^a &= U_t[(C_1^a + C_2^a y)\cosh(\omega y) + (C_3^a + C_4^a y)\sinh(\omega y)]\sin(\omega x)\\ &\quad + \frac{1}{2}U_{tt}[(D_1^a + D_2^a y)\cosh(2\omega y) + (D_3^a + D_4^a y)\sinh(2\omega y)]\\ &\quad \sin(2\omega x),\end{aligned} \tag{18}$$

and for the lower fluid, it reads as

$$\begin{aligned}\psi^b &= U_t[(C_1^b + C_2^b y)\cosh(\omega y) + (C_3^b + C_4^b y)\sinh(\omega y)]\sin(\omega x)\\ &\quad + \frac{1}{2}U_{tt}[(D_1^b + D_2^b y)\cosh(2\omega y) + (D_3^b + D_4^b y)\sinh(2\omega y)]\\ &\quad sin(2\omega x).\end{aligned} \tag{19}$$

Here, C_j^γ and U_t (for the first term in each of the last two equations), and D_j^γ and U_{tt} (for the corresponding second term), where $\gamma = a, b$ and $j = 1, 2, 3, 4$, are the constants which will be determined through the specification of the boundary conditions next.

The constants C_j^γ and D_j^γ, where $\gamma = a, b$ and $j = 1, 2, 3, 4$ can be evaluated by using the following boundary conditions:

i) No-slip, no-through flow boundary condition at the lower wall:

$$u^b(x, -b) = v^b(x, -b) = 0.$$

ii) No-slip, no-through flow boundary condition at the upper wall:

$$u^a(x, a) = v^a(x, a) = 0.$$

iii) Continuity of the tangential component of the velocity at the interface:

$$u^a(x, 0) = u^b(x, 0) = U_t\sin(\omega x) + \frac{1}{2}U_{tt}\sin(2\omega x).$$

iv) No through flow boundary condition at the interface:

$$v^a(x, 0) = v^b(x, 0) = 0.$$

As a result, we obtain the following expressions:

$$C_1^b = C_1^a = 0,$$

$$C_2^b = \frac{\sinh^2(\tilde{b})}{\sinh^2(\tilde{b}) - \tilde{b}^2}, \qquad C_2^a = \frac{\sinh^2(\tilde{a})}{\sinh^2(\tilde{a}) - \tilde{a}^2},$$

$$C_3^b = \frac{-b\tilde{b}}{\sinh^2(\tilde{b}) - \tilde{b}^2}, \qquad C_3^a = \frac{-a\tilde{a}}{\sinh^2(\tilde{a}) - \tilde{a}^2},$$

$$C_4^b = \frac{\sinh(2\tilde{b}) - 2\tilde{b}}{2(\sinh^2(\tilde{b}) - \tilde{b}^2)}, \qquad C_4^a = -\frac{\sinh(2\tilde{a}) - 2\tilde{a}}{2(\sinh^2(\tilde{a}) - \tilde{a}^2)}.$$

and

$$D_1^b = D_1^a = 0,$$

$$D_2^b = \frac{\sinh^2(2\tilde{b})}{\sinh^2(2\tilde{b}) - 4\tilde{b}^2}, \qquad D_2^a = \frac{\sinh^2(2\tilde{a})}{\sinh^2(2\tilde{a}) - 4\tilde{a}^2},$$

$$D_3^b = \frac{-2b\tilde{b}}{\sinh^2(2\tilde{b}) - 4\tilde{b}^2}, \qquad D_3^a = \frac{-2a\tilde{a}}{\sinh^2(2\tilde{a}) - 4\tilde{a}^2},$$

$$D_4^b = \frac{\sinh(4\tilde{b}) - 4\tilde{b}}{2(\sinh^2(2\tilde{b}) - 4\tilde{b}^2)}, \qquad D_4^a = -\frac{\sinh(4\tilde{a}) - 4\tilde{a}}{2(\sinh^2(2\tilde{a}) - 4\tilde{a}^2)}.$$

where $\tilde{a} = a\omega$ and $\tilde{b} = b\omega$.

Lastly, by applying the following fifth boundary condition corresponding to the Marangoni stress balance condition at the interface, which is applied to both parts of the solution for $\psi(x, y)$ given above simultaneously, the proportionality constants U_t and U_{tt} can be obtained in terms of the other constants and dimensionless parameters given above:

v) Balance of net viscous shear stress and Marangoni stress:

$$\begin{aligned}&\mu_b\frac{\partial u^b}{\partial y}\bigg|_{y=0} - \mu_a\frac{\partial u^a}{\partial y}\bigg|_{y=0}\\ &= \left\{\sigma_T + 2\sigma_{TT}[T(x, y=0) - T_{ref}]\right\}\frac{\partial T}{\partial x}\bigg|_{y=0}.\end{aligned}$$

Then, the expression for U_t reads as

$$\begin{aligned}U_t &= -\left(\frac{\Delta T}{\mu_b}\right)g(\tilde{a}, \tilde{b}, \tilde{k})h(\tilde{a}, \tilde{b}, \tilde{\mu})\\ &\quad \left[\sigma_T + 2\sigma_{TT}\left(\frac{T_c\tilde{k}b + T_h a}{(a + b\tilde{k})} - T_{ref}\right)\right],\end{aligned} \tag{20}$$

where

$$g(\tilde{a}, \tilde{b}, \tilde{k}) = \sinh(\tilde{a})f(\tilde{a}, \tilde{b}, \tilde{k}).$$

Here, the function $f(\tilde{a}, \tilde{b}, \tilde{k})$ is given in Eq. (61), and $h(\tilde{a}, \tilde{b}, \tilde{\mu})$ in Eq. (20) reads as

$$h(\tilde{a}, \tilde{b}, \tilde{\mu}) = \frac{\left(\sinh^2(\tilde{a}) - \tilde{a}^2\right)\left(\sinh^2(\tilde{b}) - \tilde{b}^2\right)}{\tilde{\mu}\left(\sinh^2(\tilde{b}) - \tilde{b}^2\right)(\sinh(2\tilde{a}) - 2\tilde{a}) + \left(\sinh^2(\tilde{a}) - \tilde{a}^2\right)\left(\sinh(2\tilde{b}) - 2\tilde{b}\right)}.$$

Moreover, the functional relationship for U_{tt} is given by

$$U_{tt} = -\left(\frac{\sigma_{TT}\Delta T^2}{\mu_b}\right)g^2(\tilde{a}, \tilde{b}, \tilde{k})\tilde{h}_1(\tilde{a}, \tilde{b}, \tilde{\mu}), \tag{21}$$

where

$$\begin{aligned}&\tilde{h}_1(\tilde{a}, \tilde{b}, \tilde{\mu})\\ &= \frac{\left(\sinh^2(2\tilde{a}) - 4\tilde{a}^2\right)\left(\sinh^2(2\tilde{b}) - 4\tilde{b}^2\right)}{\tilde{\mu}\left(\sinh^2(2\tilde{b}) - 4\tilde{b}^2\right)(\sinh(4\tilde{a}) - 4\tilde{a}) + \left(\sinh^2(2\tilde{a}) - 4\tilde{a}^2\right)\left(\sinh(4\tilde{b}) - 4\tilde{b}\right)}.\end{aligned}$$

That is, $\tilde{h}_1(\tilde{a}, \tilde{b}, \tilde{\mu}) = \tilde{h}(2\tilde{a}, 2\tilde{b}, \tilde{\mu})$. Finally, substituting for the constants in Eqs. (18) and (19), we can arrive at the following analytical solution for the stream function in the upper and lower fluids:

$$\begin{aligned}\psi^a &= \frac{U_t/\omega}{\sinh^2(\tilde{a}) - \tilde{a}^2} \times \left\{\sinh^2(\tilde{a})(\omega y)\cosh(\omega y)\right.\\ &\quad \left. - \frac{1}{2}\left[2\tilde{a}^2 + (\sinh(2\tilde{a}) - 2\tilde{a})(\omega y)\right]\sinh(\omega y)\right\}\sinh(\omega y)\end{aligned}$$

$$
\begin{aligned}
&+\frac{1}{2}\frac{U_{tt}/\omega}{\sinh^2(2\tilde{a})-4\tilde{a}^2}\times\Big\{\sinh^2(2\tilde{a})(\omega y)\cosh(2\omega y)\\
&-\frac{1}{2}\Big[4\tilde{a}^2+(\sinh(4\tilde{a})-4\tilde{a})(\omega y)\Big]\sinh(2\omega y)\Big\}\sinh(2\omega y),
\end{aligned}
$$

and

$$
\begin{aligned}
\psi^b = {}& \frac{U_t/\omega}{\sinh^2(\tilde{b})-\tilde{b}^2}\times\Big\{\sinh^2(\tilde{b})(\omega y)\cosh(\omega y)\\
&-\frac{1}{2}\Big[2\tilde{b}^2-\big(\sinh(2\tilde{b})-2\tilde{b}\big)(\omega y)\Big]\sinh(\omega y)\Big\}\sinh(\omega y).\\
&+\frac{1}{2}\frac{U_{tt}/\omega}{\sinh^2(2\tilde{b})-4\tilde{b}^2}\times\Big\{\sinh^2(2\tilde{b})(\omega y)\cosh(2\omega y)\\
&-\frac{1}{2}\Big[4\tilde{b}^2-\big(\sinh(4\tilde{b})-4\tilde{b}\big)(\omega y)\Big]\sinh(2\omega y)\Big\}\sinh(2\omega y).
\end{aligned}
$$

In addition, the analytical solutions for thermocapillary-driven velocity field components in SRFs $u^\gamma(x,y)$ and $v^\gamma(x,y)$ (for $\gamma=a,b$) can be recovered from the stream function via Eq. (13), i.e., using $u^\gamma=-\partial\psi^\gamma/\partial y$ and $v^\gamma=-\partial\psi^\gamma/\partial x$, which yields the following for the upper fluid

$$
\begin{aligned}
u^a(x,y) = {}& U_t\{[C_2^a+\omega(C_3^a+C_4^a y)]\cosh(\omega y)\\
&+(C_4^a+\omega C_2^a y)\sinh(\omega y)\}\sin(\omega x)\\
&+\frac{1}{2}U_{tt}\{[D_2^a+2\omega(D_3^a+D_4^a y)]\cosh(2\omega y)\\
&+(D_4^a+2\omega D_2^a y)\sinh(2\omega y)\}\sin(2\omega x),
\end{aligned}
$$

$$
\begin{aligned}
v^a(x,y) = {}& -\omega U_t[C_2^a y\cosh(\omega y)+(C_3^a+C_4^a y)\sinh(\omega y)]\\
&\cos(\omega x)-\omega U_{tt}[D_2^a y\cosh(2\omega y)+(D_3^a+D_4^a y)\\
&\sinh(2\omega y)]\cos(2\omega x),
\end{aligned}
\tag{22}
$$

and for the lower fluid as

$$
\begin{aligned}
u^b(x,y) = {}& U_t\{[C_2^b+\omega(C_3^b+C_4^b y)]\cosh(\omega y)\\
&+(C_4^b+\omega C_2^b y)\sinh(\omega y)\}\sin(\omega x)\\
&+\frac{1}{2}U_{tt}\{[D_2^b+2\omega(D_3^b+D_4^b y)]\cosh(2\omega y)\\
&+(D_4^b+2\omega D_2^b y)\sinh(2\omega y)\}\sin(2\omega x),
\end{aligned}
$$

$$
\begin{aligned}
v^b(x,y) = {}&\text{‘}\ -\omega U_t[C_2^b y\cosh(\omega y)+(C_3^b+C_4^b y)\sinh(\omega y)]\\
&\cos(\omega x)-\omega U_{tt}\Big[D_2^b y\cosh(2\omega y)\\
&+(D_3^b+D_4^b y)\sinh(2\omega y)\Big]\cos(2\omega x).
\end{aligned}
\tag{23}
$$

From Eqs. (22), (23), it can be inferred that the parameters U_t and U_{tt} represent measures of the scales for the thermocapillary velocity contributions arising from the linear and quadratic part of the surface tension variation with the temperature $\sigma(T)$ for the SRFs. When the coefficient σ_{TT} for the quadratic contribution in $\sigma(T)$ becomes zero (see Eq. (4)), the above results reduce to that presented in Pendse and Esmaeeli [10] applicable for the NFs.

4. Computational modeling for LBM: interface capturing and motion of binary fluids driven by thermocapillary effects

We will now discuss a modeling formulation suitable for the development of a numerical approach based on the LBM for simulation of thermocapillary convection in SRFs presented in the next section. The phase-field lattice Boltzmann approach based on the conservative Allen-Cahn equation (ACE) [54] is considered in this study to capture interfacial dynamics, which is an improvement over an earlier model [55] based on a counter term approach [56]. The binary fluids are distinguished by an order parameter or the phase field variable ϕ. The fluid A is identified by $\phi=\phi_A$, while fluid B by $\phi=\phi_B$. The interface-tracking equation based on the conservative ACE in terms of the phase field variable is given as

$$
\frac{\partial\phi}{\partial t}+\nabla\cdot(\phi\boldsymbol{u})=\nabla\cdot[M_\phi(\nabla\phi-\theta\boldsymbol{n})],
\tag{24}
$$

where $\boldsymbol{u}$ is the fluid velocity, M_ϕ is the mobility, and $\boldsymbol{n}$ is the unit normal vector, which can be calculated using the order parameter ϕ as $\boldsymbol{n}=\nabla\phi/|\nabla\phi|$. Here, the parameter θ can be expressed as $\theta=-4(\phi-\phi_A)(\phi-\phi_B)/[W(\phi_A-\phi_B)]$, where W is the width of the interface. Essentially, the term $M_\phi\theta\boldsymbol{n}$ in Eq. (24) serves as the interface sharpening term counteracting the diffusive flux $-M_\phi\nabla\phi$ following the advection of ϕ by the fluid velocity.

Now, for ease of implementations, the interfacial surface tension effects can be incorporated within a diffuse interface via a distributed or smoothed volumetric force term in a single-field formulation representing the motion of binary fluids. Then, the corresponding single-field incompressible Navier-Stokes equations for binary fluids can be written as

$$
\nabla\cdot\boldsymbol{u}=0,
\tag{25}
$$

$$
\rho\left(\frac{\partial\boldsymbol{u}}{\partial t}+\nabla\cdot(\boldsymbol{u}\boldsymbol{u})\right)=-\nabla p+\nabla\cdot\Big[\mu(\nabla\boldsymbol{u}+\nabla\boldsymbol{u}^\dagger)\Big]+\boldsymbol{F}_s+\boldsymbol{F}_{ext},
\tag{26}
$$

where $\boldsymbol{F}_s$ is the surface tension force, and $\boldsymbol{F}_{ext}$ is any external body force. Here, the surface tension force effectively exerts itself in both the normal and tangential directions to the interface as surface tension varies with temperature. To accommodate this, a geometric technique known as the continuous surface force approach [57] can be used, which can be expressed by the following equation involving the Dirac delta function δ_s:

$$
\boldsymbol{F}_s=\big(\sigma\kappa\boldsymbol{n}+\nabla_s\sigma\big)\delta_s,
\tag{27}
$$

where $\boldsymbol{n}$ and $\boldsymbol{\kappa}$ are the unit vector normal and the interface curvature, respectively; they can be obtained from the order parameter via $\boldsymbol{n}=\nabla\phi/|\nabla\phi|$ and $\kappa=\nabla\cdot\boldsymbol{n}$. In the right side of Eq. (27), the first term is the normal or capillary force, and the second term involving the surface gradient operator ∇_s is the tangential or Marangoni force. One formulation of δ_s, which localizes the smoothed surface tension force suitable within the phase-field modeling framework and thus satisfying $\int_{-\infty}^{+\infty}\delta_s dy=1$ is given by $\delta_s=1.5W|\nabla\phi|^2$.

The surface gradient ∇_s in Eq. (27) is given by $\nabla_s=\nabla-\boldsymbol{n}(\boldsymbol{n}\cdot\nabla)$. Therefore, the Cartesian components of the surface tension force in Eq. (27) can then be expressed as

$$
\begin{aligned}
F_{sx} = {}& -\sigma(T)|\nabla\phi|^2(\nabla\cdot\boldsymbol{n})n_x+|\nabla\\
&\phi|^2\Big[(1-n_x^2)\partial_x\sigma(T)-n_xn_y\partial_y\sigma(T)\Big],\\
F_{sy} = {}& -\sigma(T)|\nabla\phi|^2(\nabla\cdot\boldsymbol{n})n_y+|\nabla\phi|^2\\
&\Big[(1-n_y^2)\partial_y\sigma(T)-n_xn_y\partial_x\sigma(T)\Big].
\end{aligned}
\tag{28}
$$

Here, the functional dependence of the surface tension on temperature for the SRF is obtained from the nonlinear (parabolic) equation given in Eq. (4). In numerical implementations, in this work, the required spatial gradients $\partial_x\sigma(T)$ and $\partial_y\sigma(T)$ in Eq. (28) are calculated using an isotropic finite differencing scheme [58]. Here, we note that the temperature field T is computed by solving the energy transport equation given earlier in Eq. (3c). Finally, the jumps in fluid properties across the interface, such as density and viscosity can be expressed as a continuous function of the phase field variable, and use the following linear interpolation to account for the interfacial variations of fluid properties in this study (see e.g., Ding et al. [59]):

$$\rho = \rho_B + \frac{\phi - \phi_A}{\phi_A - \phi_B}(\rho_A - \rho_B), \quad \mu = \mu_B + \frac{\phi - \phi_A}{\phi_A - \phi_B}(\mu_A - \mu_B), \tag{29}$$

where ρ_A, ρ_B and μ_A, μ_B are the densities and the dynamic viscosities in the fluid phases, respectively and denoted by ϕ_A and ϕ_A. An equation similar to Eq. (29) will also be utilized for distributing the interfacial jump in the thermal conductivity in solving the energy equation. In this study, we use $\phi_A = 0$ and $\phi_B = 1$.

The numerical algorithms based on LB schemes using central moments for interface tracking, two fluid motion, and energy transport are presented in Appendix A with additional attendant details in Appendix B.

5. Numerical validation

5.1. Thermocapillary migration of a droplet of a normal fluid under a temperature gradient

The first validation problem that we consider is the thermocapillary migration of a droplet of a normal fluid in the field of a linear variation in temperature or a uniform gradient in temperature. Young et al. [4] presented an analytical solution of the droplet migration velocity in the creeping flow limit and at small Marangoni numbers. Taking $\sigma(T) = \sigma_0 + \sigma_T(T - T_{ref})$ for the surface tension variation, consider a droplet of radius R with a density ρ_b, viscosity μ_b, and thermal conductivity k_b in the presence of a uniform temperature gradient ∇T_∞, then the characteristic velocity U_* obtained under a balance of the thermocapillary force and the viscous force can be written as

$$U_* = -\frac{\sigma_T |\nabla T_\infty| R}{\mu_b}. \tag{30}$$

Defining the Reynolds number and the Marangoni number as $\mathrm{Re} = \rho_b U_* R/\mu_b$ and $\mathrm{Ma} = U_* R/k_b$, respectively, in the limit $Re \ll 1$ and $Ma \ll 1$, Young et al. performed a theoretical analysis and derived an expression for the terminal migration velocity of the droplet U_{YGB} given by

$$U_{YGB} = \frac{2U_*}{(2+\tilde{k})(2+3\tilde{\mu})}, \tag{31}$$

where $\tilde{k}$ and $\tilde{\mu}$ are the property ratios defined in Eq. (6).

For performing the numerical simulation using the LB schemes presented in the previous sections, here and in what follows for the rest of this paper, when required, the no-slip velocity boundary condition is prescribed using the standard half-way bounce-back condition, while the specification of the scalar field such as the temperature on the boundaries is carried out using the anti-bounce back scheme; the no-gradient conditions on any boundary are imposed using the free-slip condition; finally, as is typical for the LB method, all the values are specified in the lattice units. See Ref. [60] for further details.

We consider a droplet of radius $R = 20$ initially kept at the center of a 2D domain of size $8R \times 16R$. No slip boundary conditions are imposed on the top and bottom walls while periodic boundary conditions are used on the left and right walls. In the direction normal to the bottom and top walls, a linear variation in the temperature field with $T_{bot} = 0$ on the bottom wall and $T_{top} = 32$ on the top wall is imposed, resulting in a constant temperature gradient in the far field $\nabla T_\infty = 0.1$. For the fluid properties, we take $\rho_{a,b} = c_{p_{a,b}} = 1$, $\mu_{a,b} = k_{a,b} = 0.2$, $T_{ref} = 16$, $\sigma_0 = 2.5 \times 10^{-3}$, and $\sigma_T = -10^{-4}$ and the values of the parameters are such that the assumption of the negligible convection in deriving the analytical solution is satisfied. For the above choice, the theoretically predicted value of the terminal velocity of the droplet is $U_{YGB} = 1.333 \times 10^{-4}$, and both Re and Ma are 0.1.

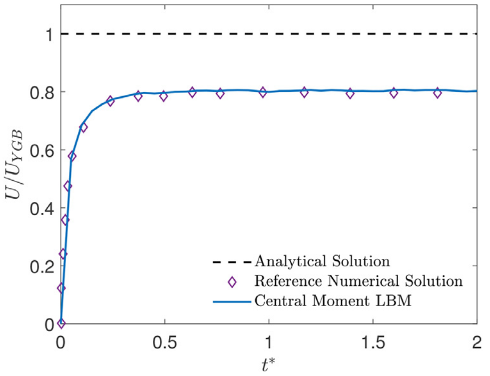

Fig. 3. The drop migration velocity for a 2D droplet at Re = Ma = 0.1 normalized by the analytical prediction velocity U_{YGB} versus the dimensionless time $t^* = tU/R$. The other reference numerical solution for a 2D droplet is taken from Ref. [61].

Figure 3 shows the temporal variations of the normalized drop migration velocity U/U_{YGB} as a function of the dimensionless time $t^* = tU/R$ computed using the LB schemes presented earlier along with the theoretical prediction, as well as results from another reference numerical solution involving a 2D droplet [61]. It should be noted that the theory assumed a 3D axisymmetric, non-deformable spherical droplet, while the present LB results as well as the reference numerical results are based on considering a 2D droplet. As a result, all the numerical schemes shown consistently attain $U/U_{YGB} \approx 0.80$ or about 80% of the theoretical value. Nevertheless, the present results are in good quantitative agreement with the reference results given in Guo and Lin [61] for similar conditions. Moreover, this trend is also consistent with the results obtained by the use of different numerical methods for this problem involving a 2D droplet (see e.g., Guo and Lin [61], Zheng et al. [62], Nabavizadeh et al. [63]).

5.2. Thermocapillary-driven flow in a heated microchannel with two superimposed normal fluids

As a second benchmark problem, we will test our LB schemes for the simulation of the thermocapillary-driven flow in a sinusoidally heated microchannel which confines two supperimposed normal fluids (NFs) [10]. The problem setup for this case is the same as the one presented in Section 2.1 (see Fig. 2 for the geometric set up). The wall temperatures are applied according to Eqs. (1) and (2). The dimensionless parameters Re, Ma, and Ca for this case are defined in Eq. (5) and the ratio of the material properties are given in Eq. (6). For $Re \ll 1$, $Ma \ll 1$, and $Ca \ll 1$, and considering the flow is driven by a surface tension gradient, where the surface tension decreases linearly with the increasing temperature for the NF as $\sigma(T) = \sigma_0 + \sigma_T(T - T_{ref})$, Ref. [10] derived analytical solutions for the temperature $T(x, y)$, stream function $\psi(x, y)$, and the components of the velocity field $u(x, y)$ and $v(x, y)$. It can also be obtained as a special case of the analytical solution derived in this work by setting the coefficient for the quadratic term for the surface tension variation with temperature to be zero, i.e., $\sigma_{TT} = 0$.

We performed LB simulations by considering two normal fluids of equal thickness $a = b = 50$ in a microchannel of length $l = 200$. Periodic boundary conditions are used on the left and right sides of the domain, while no-slip boundary conditions are imposed on the top and bottom walls, and the wall temperatures are applied using Eqs. (1) and (2) with $T_h = T_c = T_{ref} = \Delta T = 1.0$ for simplicity.

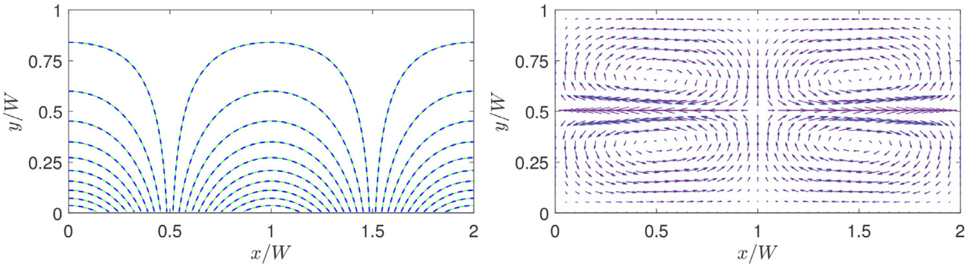

(a) Temperature contours (b) Velocity vectors

Fig. 4. (a) Temperature contours of the NF in thermocapillary flow within a heated microchannel with thermal conductivity ratio $\tilde{k}=1$ and viscosity ratio $\tilde{\mu}=1$ obtained from the LB simulation results (solid green lines) and the analytical solution (dashed blue lines). (b) Velocity vectors due to thermocapillary flow of the NF obtained from the LB simulation results (blue arrows) and the analytical solution (purple arrows). (For interpretation of the references to color in this figure legend, the reader is referred to the web version of this article.)

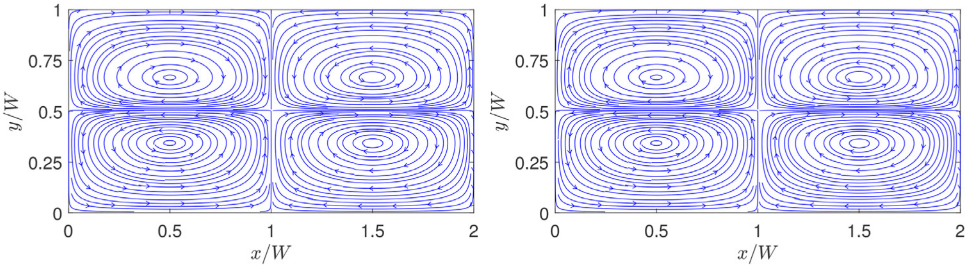

(a) Analytical Solution (b) LBM Simulation

Fig. 5. Streamlines of the thermocapillary flow in NFs within a heated microchannel with thermal conductivity ratio $\tilde{k}=1$ and viscosity ratio $\tilde{\mu}=1$ obtained from the analytical solution (left) and the LB simulation results (right). The arrows indicate the direction of the thermocapillary convection.

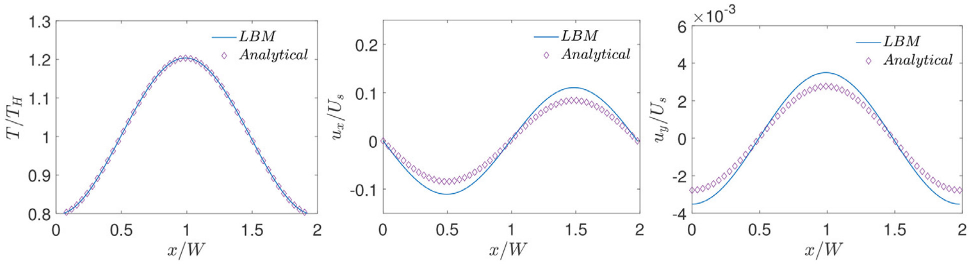

Fig. 6. Profiles of the temperature and velocity components along the centerline of the domain in the x direction for thermocapillary flow of a NF in a heated microchannel. The purple diamond symbols shown are obtained from the analytical solution given by Pendse and Esmaeeli [10] and the blue lines are the LB simulation results. (For interpretation of the references to color in this figure legend, the reader is referred to the web version of this article.)

The various fluid properties are chosen as follows: $\sigma_0 = 1.0 \times 10^{-2}$, $M_1 = -5.0 \times 10^{-2}$, $M_2 = 0$, $\tilde{k} = 1$, and $\tilde{\mu} = 1$; moreover, the dimensionless parameters are $\mathrm{Re} = 1.59 \times 10^{-1}$, $\mathrm{Ma} = 3.83 \times 10^{-2}$, and $\mathrm{Ca} = 1.26 \times 10^{-2}$, so that the assumptions made in deriving the analytical solution are satisfied. For the phase-field model, the values of the interface thickness and the mobility parameter are $W = 5$ and $M_\phi = 0.02$, respectively.

Figure 4 (a) shows the equispaced contours of the temperature field for $\tilde{k} = 1$ and $\tilde{\mu} = 1$ obtained by the LB simulation as well as from the analytical solution [10]; Moreover, Fig. 4(b) provides a similar comparison of the thermocapillary velocity vectors which shows that the fluid motion occurring in the direction away from the higher temperature zones on the interface as would be expected for NFs. Clearly, the simulation results agree well with the analytical solution. The overall flow pattern for the thermocapillary convection in NFs is shown in Fig. 5, which consists of four periodic counter-rotating vortices in the two superimposed fluids. The numerical results based on the LB schemes are seen to be qualitatively consistent with the analytical solution [10] for the streamline contours. Finally, Figs. 6 and 7 present quantitative comparisons between our numerical approach and the analytical solution for the profiles of the temperature and the components of the thermocapillary velocity field along the centerlines of the domain in both the horizontal (x) and vertical (y) directions, respectively. In these figures, the temperature profiles are non-dimensionalized using the bottom wall temperature, while the velocity profiles are normalized using a characteristic velocity scale U_s given in Eq. (32) by setting $\sigma_{TT} = 0$ which is appropriate for NFs considered here. Again, they are fairly in good agreement with each other, thereby validating the implementation of our LB schemes presented earlier.

6. Results and discussion

We will now study the effect of various characteristic parameters on the physics of thermocapillary convection in superimposed layers of two self-rewetting fluids (SRFs) confined with a microchannel, where the bottom wall is nonuniformly heated by imposing a sinusoidal variation in temperature, while the top wall is maintained at a lower, but uniform temperature (see Fig. 2). In this regard, we will utilize the new analytical solution developed in Section 3 and consider cases, where the quadratic coefficient

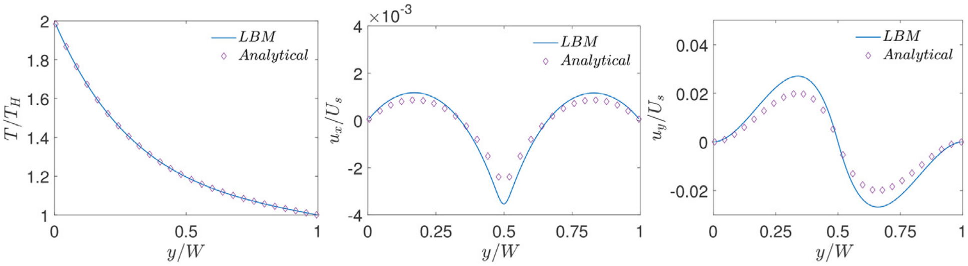

Fig. 7. Profiles of the temperature and velocity components along the centerline of the domain in the y direction for thermocapillary flow of a NF in a heated microchannel. The purple diamond symbols shown are obtained from the analytical solution given by Pendse and Esmaeeli [10] and the blue lines are the LB simulation results. (For interpretation of the references to color in this figure legend, the reader is referred to the web version of this article.)

of the surface tension variation with the temperature is non-zero, i.e., $\sigma_{TT} \neq 0$ or $M_2 \neq 0$ to demonstrate the role of SRFs, and compare both the qualitative and quantitative differences in their behavior when compared with the normal fluids, where only the linear coefficient exists. Also, the LB schemes, which were validated in the previous section, will be used in conjunction with the analytical solution for providing additional confirmation of the applicability as well as for ensuring quantitative accuracy of the latter via numerical simulations of thermocapillary-driven flows in SRFs. For clarification, it suffices to mention that three distribution functions are used in our LB formulation to compute the two-fluid motion, interface capturing, as well as the transport of the energy within the SRFs. The temperature-dependent surface tension, which is used as a regularized volumetric body force in a single-field formulation for the fluid motion is used to couple the latter with the temperature field. The values of the bulk fluid properties such as the viscosity and the thermal conductivity are chosen such that the resulting flow and transport occurs in the creeping regime and at small Marangoni and capillary numbers (i.e., Re $\ll 1$, Ma $\ll 1$, and Ca $\ll 1$) in numerical simulations, where the latter also ensures that the interface is naturally maintained as flat, which is valid in situations in microchannel flows.

We perform simulations in a 2D computational domain with 200×100, thereby the length l of the microchannel is 200 and the total thickness of both the SRFs $(a+b)$ is 100. Periodic boundary conditions are used in the horizontal direction, while no-slip boundary conditions are imposed on the top and bottom walls, and the wall temperatures are applied from Eqs. (1) and (2) where we choose $T_h = T_c = T_{ref} = \Delta T = 1.0$ for simplicity. The reference surface tension is taken is $\sigma_0 = 1 \times 10^{-2}$. Thermocapillary flow patterns and their strengths are determined by the choice of the dimensionless linear and quadratic coefficients of the surface tension variation with temperature, i.e., M_1 and M_2, respectively. For the model parameters in the conservative ACE for interface tracking, we chose $W = 5$ and $M_\phi = 0.02$.

First, we consider cases with two superimposed fluids having the same thickness or $a/b = 1$ and with property ratios $\tilde{k} = 1$ and $\tilde{\mu} = 1$. To provide a perspective and a basis for comparison, we will first show the streamlines for a case with NFs in Fig. 8 by considering $M_1 = -5 \times 10^{-2}$ and $M_2 = 0.0$. We treat these choices for the dimensionless surface tension coefficients as the baseline case for NFs. Moreover, the choices of the other fluid properties are such that Re $= 1.59 \times 10^{-1}$, Ma $= 3.83 \times 10^{-2}$, and Ca $= 1.26 \times 10^{-2}$. In defining these dimensionless parameters here and in what follows, a characteristic velocity U_s derived in Appendix D is used. Clearly, if the quadratic coefficient for the surface tension is absent (i.e., $\sigma_{TT} = 0$ or $M_2 = 0$), then *four periodic counterrotating vortices* are induced, where the fluids *move away from the hotter region on the interface* at the center of the domain.

On the other hand, by turning off the linear coefficient of surface tension (i.e., $\sigma_T = 0$) and keeping only the quadratic coefficient non-zero, i.e., $\sigma_{TT} \neq 0$, for otherwise the same property ratios, we simulate the thermocapillary convection in SRFs. In dimensionless form, we take $M_1 = 0$ and $M_2 = 1 \times 10^{-1}$, which we consider as the choices for the baseline case for SRFs; the rest of the dimensionless parameters resulting from specifying the other fluid properties are Re $= 1 \times 10^{-1}$, Ma $= 3 \times 10^{-2}$, and Ca $= 9.9 \times 10^{-3}$. The results given in terms of the streamlines are plotted in Fig. 9. It is evident that the thermocapillary flow pattern in SRFs is strikingly different from that in NFs: First, *eight periodic counterrotating vortices* are generated in SRFs, which is double the number of the convection rolls in NFs. Second, the fluids on the interface seek to *move towards the hotter region on the interface* at the center of the domain. Such differences in direction of the thermocapillary flow fields between the NFs and SRFs are more explicit in the velocity vector diagrams shown in Fig. 10, which is a manifestation of flow arising from the Marangoni stress generated due to a positive (negative) surface tension gradient on the interface for SRFs (NFs). The doubling of the vortical structures in the case of the SRFs can be interpreted from an earlier and simpler form of the analytical solution given in terms of the streamfunction in Eq. (16): this equation contains the 'fundamental solution' related to $\sin(\omega x)$ arising from the linear part surface tension coefficient σ_T and a 'first order harmonic solution' related to $\sin(\omega x)\cos(\omega x)$ generated from the quadratic part surface tension coefficient σ_{TT}. The latter is of the form $\sin(2\omega x)/2$, which has double the wavenumber compared to the former case. Thus, fluids with surface tension such that $\sigma_{TT} \neq 0$ (or SRFs) would result in double the number of thermocapillary convection rolls when compared to fluids with only linear variations in the surface tension, i.e., only $\sigma_T \neq 0$ (or NFs).

Finally, we note that in all cases, the side-by-side comparisons between the analytical solution and the numerical results based on the LB schemes show very good agreement with each other.

6.1. Effect of relative magnitudes of dimensionless linear M_1 and quadratic M_2 surface tension coefficients of SRF layers

In the previous case, we considered a particular type of SRF for which only the quadratic coefficient is non-zero, while the linear part of the coefficient is absent, i.e., $M_2 \neq 0$, but $M_1 = 0$. While this is a plausible assumption, it doesn't encompass all types of SRFs, for which it is possible to have both $M_2 \neq 0$ and $M_1 \neq 0$, and the unique nature of the flow patterns associated with the SRFs can still be manifested provided that the overall surface tension gradient is positive in the flow domain of interest. To test this hypothesis, we used the following parameters for SRFs with both the linear and quadratic coefficients: $\sigma_0 = 1 \times 10^{-3}$, $M_1 = 1 \times 10^{-5}$, and $M_2 = 5 \times 10^{-1}$. Based on such more general forms of surface tension coefficients, results from the analytical solution and well as the LB simulations are obtained and the corresponding thermocapillary convection patterns given in terms of the streamlines are presented in Fig. 11. Again, we notice here that eight counterrotat-

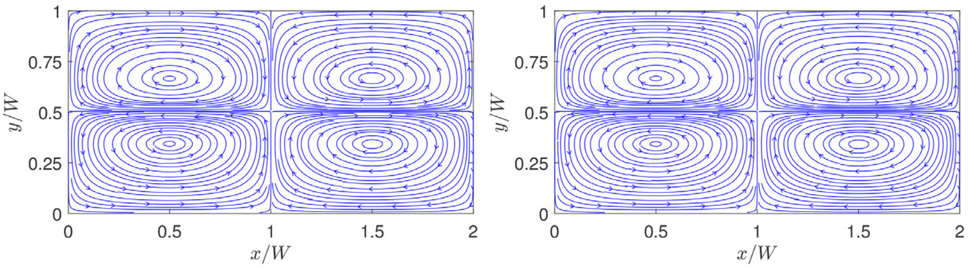

(a) Analytical Solution (b) LBM Simulation

Fig. 8. Comparison of the streamlines between the analytical solution with the LBM simulation of thermocapillary convection in NFs for the case of aspect ratio of $a/b = 1$, thermal conductivity ratio of $\tilde{k} = 1$, and viscosity ratio of $\tilde{\mu} = 1$. Here, the dimensionless linear and quadratic coefficients of surface tension variation with temperature are $M_1 = -5 \times 10^{-2}$ and $M_2 = 0$, respectively.

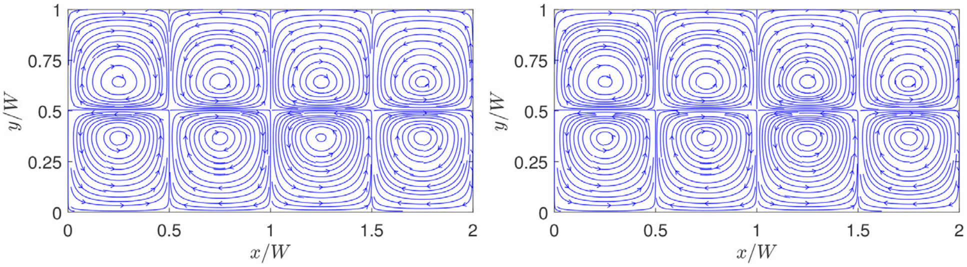

(a) Analytical Solution (b) LBM Simulation

Fig. 9. Comparison of the streamlines between the analytical solution with the LBM simulation of thermocapillary convection in SRFs for the case of aspect ratio of $a/b = 1$, thermal conductivity ratio of $\tilde{k} = 1$, and viscosity ratio of $\tilde{\mu} = 1$. Here, the dimensionless linear and quadratic coefficients of surface tension variation with temperature are $M_1 = 0$ and $M_2 = 1 \times 10^{-1}$, respectively.

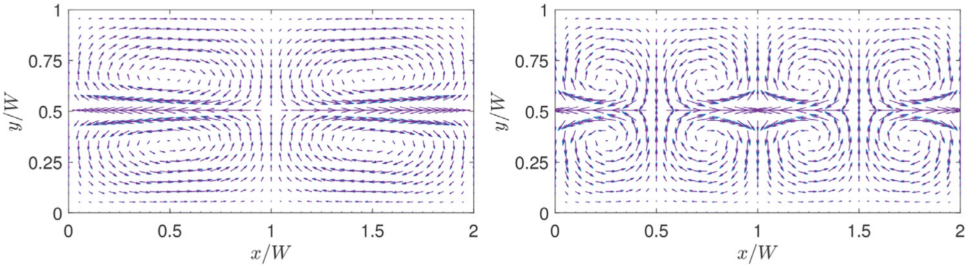

(a) Normal Fluid (b) Self Re-wetting Fluid

Fig. 10. Velocity vectors due to thermocapillary convection for the case of (a) NFs ($M_1 = -5 \times 10^{-2}$ and $M_2 = 0$) and (b) SRFs ($M_1 = 0$ and $M_2 = 1 \times 10^{-1}$). Here, the aspect ratio is $a/b = 1$, thermal conductivity ratio is $\tilde{k} = 1$, and the viscosity ratio is $\tilde{\mu} = 1$. The blue arrows are for the LBM simulation while the purple arrows are for the analytical solution. (For interpretation of the references to color in this figure legend, the reader is referred to the web version of this article.)

ing convection rolls are generated, where the fluid motion along the interface is directed towards the higher temperatures, which confirms our hypothesis mentioned above. Moreover, the theoretical prediction is consistent with the numerical results based on LB schemes.

This last example concerned a situation where the dimensionless linear coefficient of surface tension is much smaller than that of the quadratic coefficient. Let's now explore another case by inverting this situation where the linear coefficient is much larger than the quadratic coefficient in SRF layers. In particular, we take $M_1 = 1 \times 10^{-1}$ and $M_2 = 1 \times 10^{-4}$, and the streamline patterns based on the analytical solution and the LBM simulation results are shown in Fig. 12. Interestingly, in this case only four periodic counterrotating vortices are generated; however, unlike those observed for the NFs in the previous section where the fluids on the interface move away from the center (see Fig. 8), here the thermocapillary motion along the interface is directed towards the higher temperature zones at the center of the microchannel, which is consistent withe expected behavior of SRFs. Now, the presence of four vortices for the present case where $M_2 \ll M_1$ and eight vortices for the previous case where $M_2 \gg M_1$ can be explained as follows. The analytical solution derived in a previous section consists of the superposition of two results: one that arises from the linear coefficient of the surface tension M_1 and the other is generated from the quadratic coefficient M_2, which contains contribution of thermocapillary flow with a wavenumber that is twice as the former case. Moreover, the resulting magnitudes of the flow in each case is proportional to the magnitude of the respective coefficient of the surface tension. Thus, the overall solution, in terms of the dominant flow pattern, is then dictated by the contribution of the part of the solution which has the largest magnitude arising between the two surface tension coefficients.

Indeed, in view of the above considerations, we performed a systematic study to deduce the parameter space $M_1 - M_2$ that delineates the cases with four vortices with those of eight vortices in SRFs. Figure 13 presents a parametric regime map in terms of the linear and quadratic surface tension coefficients, when all the other characteristic parameters are fixed as follows: $a/b = 1$, $\tilde{k} = 1$, and $\tilde{\mu} = 1$. We find for all cases where $M_2 > M_1$ with the above parametric choices, the thermocapillary convection in SRFs mani-

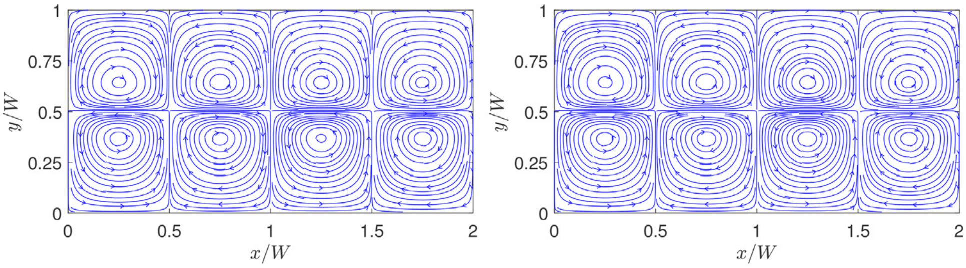

(a) Analytical Solution (b) LBM Simulation

Fig. 11. Comparison of the streamlines between the analytical solution with the LBM simulation of thermocapillary convection in SRFs for the case of aspect ratio of $a/b = 1$, thermal conductivity ratio of $\tilde{k} = 1$, and viscosity ratio of $\tilde{\mu} = 1$. Here, the dimensionless linear and quadratic coefficients of surface tension variation with temperature are $M_1 = 1 \times 10^{-5}$ and $M_2 = 5 \times 10^{-1}$, respectively.

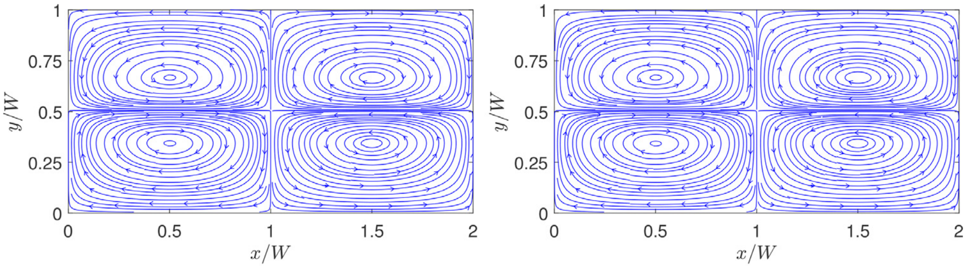

(a) Analytical Solution (b) LBM Simulation

Fig. 12. Comparison of the streamlines between the analytical solution with the LBM simulation of thermocapillary convection in SRFs for the case of aspect ratio of $a/b = 1$, thermal conductivity ratio of $\tilde{k} = 1$, and viscosity ratio of $\tilde{\mu} = 1$. Here, the dimensionless linear and quadratic coefficients of surface tension variation with temperature are $M_1 = 1 \times 10^{-1}$ and $M_2 = 1 \times 10^{-4}$, respectively.

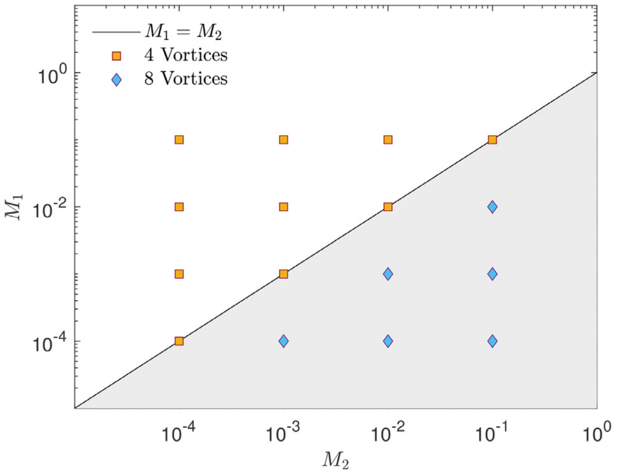

Fig. 13. Parametric regime map given in terms of the dimensionless linear M_1 and quadratic M_2 surface tension coefficients for the four and eight vortex convection roll cases induced by thermocapillary effects in SRFs in a nonuniformly heated microchannel. Here, the aspect ratio is $a/b = 1$, the thermal conductivity ratio is $\tilde{k} = 1$, and viscosity ratio is $\tilde{\mu} = 1$. The symbols correspond to our analytical prediction, with the shaded region encompassing the eight vortex cases.

fests in the form of eight counterrotating vortex cells as shown by the shaded region in Fig. 13; otherwise the SRFs exhibit four vortex cells. Moreover, unlike in NFs, the SRFs, regardless of the choice of M_1 and M_2, always seek to move towards the hotter regions at the center on the interface. These findings may be exploited in creating new pathways to specifically promote certain targeted mixing patterns in microfluidic channels subjected to nonuniform wall heating by tuning surface tension coefficients, i.e., by synthesizing SRFs with appropriate interfacial properties σ_T and σ_{TT} (or equivalently, M_1 and M_2), e.g., by selecting appropriate number of carbon atoms in the molecular chain arrangements in aqueous solutions of alcohols.

6.2. Effect of relative thickess ratio a/b of SRF layers

Next, let's examine the effect of changing the relative thicknesses a and b of the top and bottom fluids or the aspect ratio a/b on thermocapillary flow patterns for both NFs and SRFs. Figure 14 shows the streamlines in NFs when the aspect ratio $a/b = 1/3$, while the corresponding result for the SRFs is presented in Fig. 15. By contrast, Figs. 16 and 17 illustrate the streamlines in the thermocapillary-driven flow in NFs and SRFs, respectively, when the aspect ratio $a/b = 3$.

In general, changing the thickness ratio a/b does not modify the number of vortices generated either for NFs or SRFs, which are primarily influenced by the surface tension sensitivity coefficients M_1 and M_2, as discussed earlier. However, the shape of the vortices are profoundly influenced by the a/b ratio as seen in Figs. 14–17. When $a/b = 1/3$ (see Figs. 14 and 15), the interface is farther way from the heated bottom wall when compared to the previous cases with $a/b = 1$; with smaller prevailing thermal gradients this reduces the heat diffusion from the bottom to the interface and its consequent nonuniform thermal distribution; in turn, this sets up relatively weaker thermocapillary currents. Moreover, in this case with the bottom fluid being thicker, their vortical centers are also pushed farther away from the bottom wall. In the case of NF layers (see Fig. 14), the motion is directed away from the interface, while with SRF layers (see Fig. 15) the fluids seek to migrate towards the hotter zones around the center of the interface thereby setting up overall *asymmetrical* flow patterns in each case.

On the other hand, for the thickness ratio $a/b = 3$ (see Figs. 16 and 17), the interface is significantly closer to the nonuniformly heated bottom wall when compared to the above cases. As a result of greater thermal transport towards the interface, Marangoni convection becomes more intense, which is accompa-

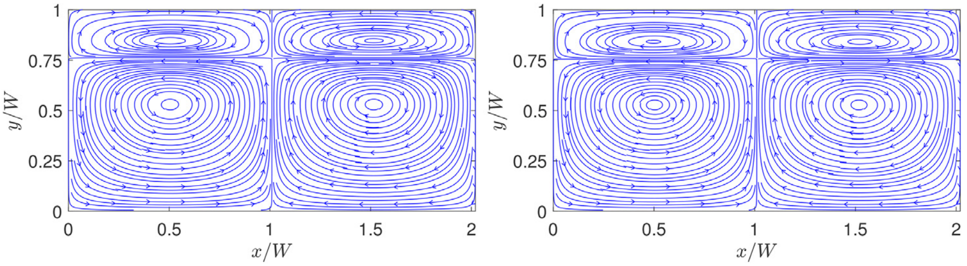

(a) Analytical Solution (b) LBM Simulation

Fig. 14. Comparison of the streamlines between the analytical solution with the LBM simulation of thermocapillary convection in NFs for the case of aspect ratio of $a/b = 1/3$, thermal conductivity ratio of $\tilde{k} = 1$, and viscosity ratio of $\tilde{\mu} = 1$. Here, the dimensionless linear and quadratic coefficients of surface tension variation with temperature are $M_1 = -5 \times 10^{-2}$ and $M_2 = 0$, respectively.

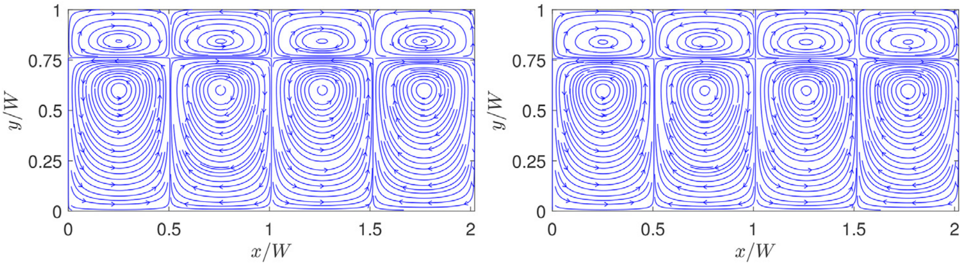

(a) Analytical Solution (b) LBM Simulation

Fig. 15. Comparison of the streamlines between the analytical solution with the LBM simulation of thermocapillary convection in SRFs for the case of aspect ratio of $a/b = 1/3$, thermal conductivity ratio of $\tilde{k} = 1$, and viscosity ratio of $\tilde{\mu} = 1$. Here, the dimensionless linear and quadratic coefficients of surface tension variation with temperature are $M_1 = 0$ and $M_2 = 1 \times 10^{-1}$, respectively.

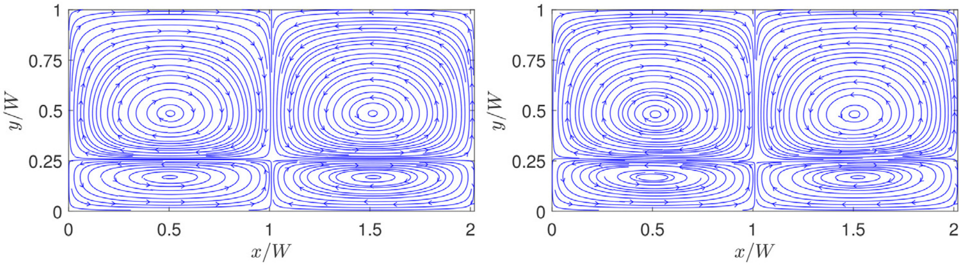

(a) Analytical Solution (b) LBM Simulation

Fig. 16. Comparison of the streamlines between the analytical solution with the LBM simulation of thermocapillary convection in NFs for the case of aspect ratio of $a/b = 3$, thermal conductivity ratio of $\tilde{k} = 1$, and viscosity ratio of $\tilde{\mu} = 1$. Here, the dimensionless linear and quadratic coefficients of surface tension variation with temperature are $M_1 = -5 \times 10^{-2}$ and $M_2 = 0$, respectively.

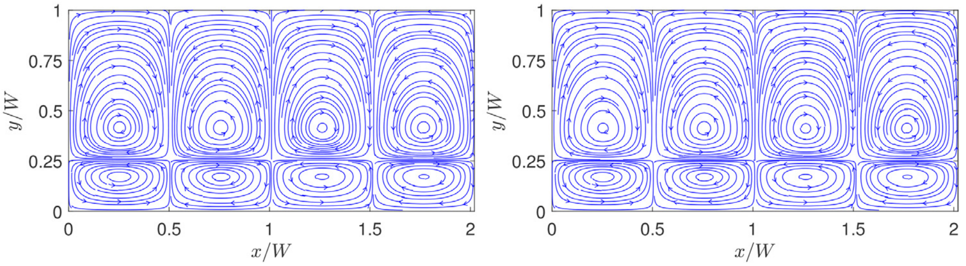

(a) Analytical Solution (b) LBM Simulation

Fig. 17. Comparison of the streamlines between the analytical solution with the LBM simulation of thermocapillary convection in SRFs for the case of aspect ratio of $a/b = 3$, thermal conductivity ratio of $\tilde{k} = 1$, and viscosity ratio of $\tilde{\mu} = 1$. Here, the dimensionless linear and quadratic coefficients of surface tension variation with temperature are $M_1 = 0$ and $M_2 = 1 \times 10^{-1}$, respectively.

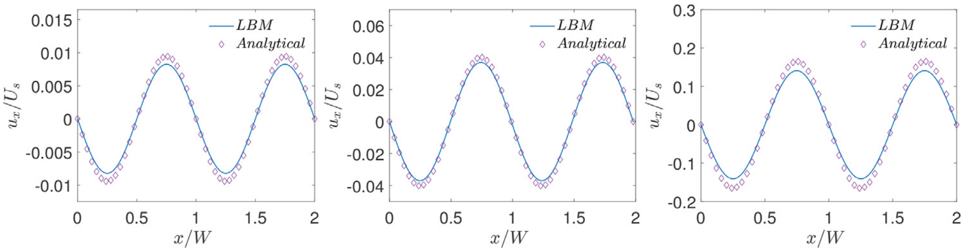

Fig. 18. Profiles of the horizontal velocity component along the interface in the x direction for thermocapillary flow in SRFs for three different values of the aspect ratio a/b: $a/b = 1/3$ (left), $a/b = 1$ (middle), and $a/b = 3$ (right). The purple diamond symbols shown are obtained from the analytical solution and the lines are the LB simulation results. Here, the thermal conductivity ratio is $\tilde{k} = 1$, viscosity ratio is $\tilde{\mu} = 1$, and the dimensionless surface tension coefficients are $M_1 = 0$ and $M_2 = 1 \times 10^{-1}$. (For interpretation of the references to color in this figure legend, the reader is referred to the web version of this article.)

nied by the centers of the bottom standing vortex cells shifting further towards the bottom wall, i.e., the corresponding flow pattern in that layer becoming more squished; nevertheless, the direction of the motion of the counterrotating vortices in such asymmetrical flow distribution for the NFs and the SRFs remains the same as mentioned above. These observations can be further interpreted more quantitatively by examining the variations in the magnitude of the interfacial thermocapillary convection currents at different a/b ratios as discussed next in Fig. 18.

Hence, by focusing on the interface, let's now investigate the variations in the distribution of the horizontal component of the thermocapillary velocity field u_x in SRFs due to changes in the aspect ratio a/b, which we will normalize by a suitable characteristic velocity arising from the surface tension gradient. Based on the scaling argument given below Eq. (7) involving a balance of the Marangoni stress and the viscous stress and using the average temperature on the interface in estimating the attendant temperature gradient, we can obtain the following characteristic velocity for thermocapillary convection in SRFs (see Appendix D for details):

$$U_s \sim \frac{\Delta T}{\mu^b}\left(\frac{b}{l}\right)\left[\sigma_T + 2\sigma_{TT}\left(\frac{T_h\left(\frac{a}{b}\right) + T_c\tilde{k}}{\left(\frac{a}{b}\right) + \tilde{k}} + \frac{\Delta T \sinh(\tilde{a})}{\tilde{k}\cosh(\tilde{a})\sinh(\tilde{b}) + \cosh(\tilde{b})\sinh(\tilde{a})} - T_{ref}\right)\right]. \tag{32}$$

Then, taking $W = a + b$ as the width of the microchannel, Fig. 18 presents the dimensionless horizontal velocity component u_x/U_s on the interface in SRFs as a function of the dimensionless coordinate x/W for three different aspect ratios $a/b = 1/3, 1$ and 3. It can be seen that while the velocity profiles are qualitatively similar, there are dramatic differences in the strength of the Marangoni convection currents in the interface depending on the aspect ratio. When the interface is far from the nonuniformly heated bottom wall, which occurs for the case $a/b = 1/3$, the magnitude of the thermocapillary convection is found to be relatively weak; by contrast, when the interface is closer to the interface at $a/b = 3$ than the other two cases, the Marangoni velocities are much larger, by at least an order of magnitude. This is consistent with our arguments given earlier that the closer the interface is to the heated wall side, the greater is the heat transport by diffusion from the latter to the former, which in turn intensifies the generation of thermocapillary velocity currents via the surface tension gradient resulting from a nonuniform temperature distribution on the interface. Thus, the aspect ratio a/b of the superimposed layers of SRFs has a major effect on not just in setting up asymmetrical thermocapillary convection roll cells, but also, and more importantly, in determining the resulting magnitude of the velocities of the fluids around interfaces. For the purpose of clarification, it should be noted that the length scale b used in determining the shear stress used in obtaining a scale for the characteristic velocity U_s (see Appendix D for its derivation), while a consistent scaling definition following [10], is an overestimate. Hence, the dimensionless velocity profiles u_x/U_s shown are generally significantly smaller than unity.

6.3. Effect of thermal conductivity ratio $\tilde{k}$ of SRF layers

Next, we will perform another quantitative study involving the effect of the thermal conductivity ratio $\tilde{k} = k_a/k_b$ on the profiles of temperature and the components of the velocity field in thermocapillary convection in SRFs. In this regard, we fix SRF layers to be of equal thickness, i.e., $a/b = 1$, and set $\tilde{\mu} = 1$, $M_1 = 0$ and $M_2 = 1 \times 10^{-1}$, and then vary $\tilde{k}$ by considering three representative choices: $\tilde{k} = 0.1, 1.0$ and 5.0. Figures 19 and 20 show the profiles of the temperature and the components of the velocity field along the centerline of the domain in the x and y directions, respectively, for $\tilde{k} = 0.1$. Similar plots are shown in Figs. 21 and 22 for $\tilde{k} = 1.0$ and in Figs. 23 and 24 for $\tilde{k} = 5.0$. First, focusing on the dimensionless temperature profiles T/T_H, we notice that $\tilde{k}$ generally does not change their overall magnitudes; however, it does change the shape of the temperature profiles in the direction vertical to the interface: while for $\tilde{k} = 1.0$ (see Fig. 22) it exhibits a continuous variation, when $\tilde{k} \neq 1$, a discontinuity in the slopes of the temperatures at the interface at $y/W = 0.5$ can be observed (see Figs. 20 and 24), which can be interpreted simply based on the continuity of the heat flux and using the Fourier's law. This also explains the observation that for the case when the top fluid layer is significantly more conducting than the bottom fluid layer (i.e., $\tilde{k} = 5.0$), the temperature field changes much more in the former when compared to the latter (see Fig. 24). More importantly, the thermal conductivity ratio has more profound influence on the magnitude of the thermocapillary flow fields. While the overall shapes of the components of the velocity fields are generally invariant with $\tilde{k}$, it can be seen that when bottom fluid is thermally more conducting, i.e., when $\tilde{k} < 1.0$, the magnitudes of the thermocapillary velocity currents are significantly increased; for example, comparing Figs. 19 and 20 (for $\tilde{k} = 0.1$) with the corresponding Figs. 23 and 24 (for $\tilde{k} = 5.0$), it can be observed that the Marangoni velocities are significantly larger for the former case when compared the latter. This is a consequence of the fact that when $\tilde{k} < 1.0$, the thermal conductivity of the bottom fluid layer is significantly larger relative to the top fluid layer thereby enhancing heat diffusion to the interface, which in turn sets up significantly larger surface tension gradient induced fluid motion. It is also consistent with the scaling equation for the characteristic thermocapillary velocity U_s given above in Eq. (32) based on a stress balance on the interface, which parameterizes it with $\tilde{k}$, among other characteristic parameters. Finally, we also note that the theoretical predictions for the temperature fields as well as the velocity fields

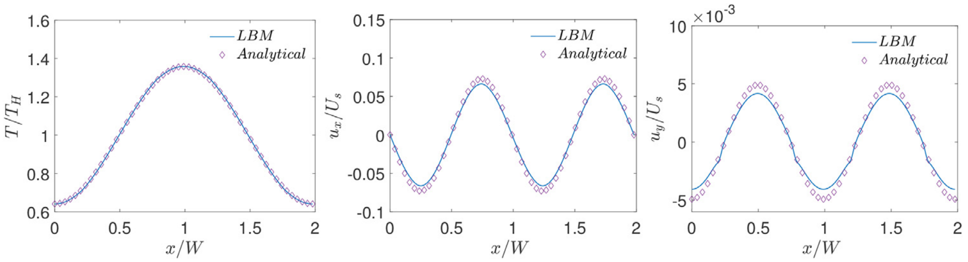

Fig. 19. Profiles of the temperature and velocity components along the centerline of the domain in the x direction for thermocapillary flow in SRFs for thermal conductivity ratio $\tilde{k} = 0.1$. The purple symbols shown are obtained from the analytical solution and the lines are the LB simulation results. Here, the aspect ratio is $a/b = 1$, viscosity ratio is $\tilde{\mu} = 1$, and the dimensionless surface tension coefficients are $M_1 = 0$ and $M_2 = 1 \times 10^{-1}$. (For interpretation of the references to color in this figure legend, the reader is referred to the web version of this article.)

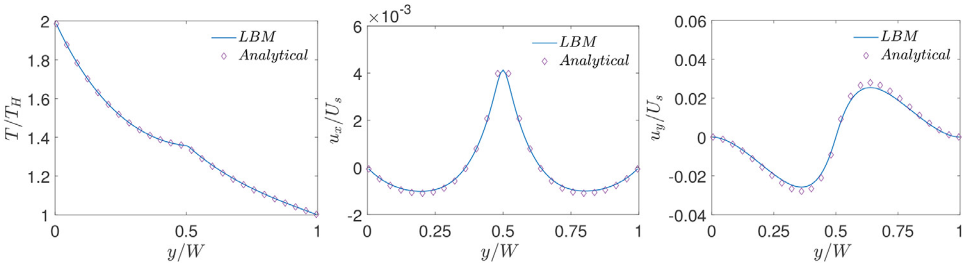

Fig. 20. Profiles of the temperature and velocity components along the centerline of the domain in the y direction for thermocapillary flow in SRFs for thermal conductivity ratio $\tilde{k} = 0.1$. The purple symbols shown are obtained from the analytical solution and the lines are the LB simulation results. Here, the aspect ratio is $a/b = 1$, viscosity ratio is $\tilde{\mu} = 1$, and the dimensionless surface tension coefficients are $M_1 = 0$ and $M_2 = 1 \times 10^{-1}$. (For interpretation of the references to color in this figure legend, the reader is referred to the web version of this article.)

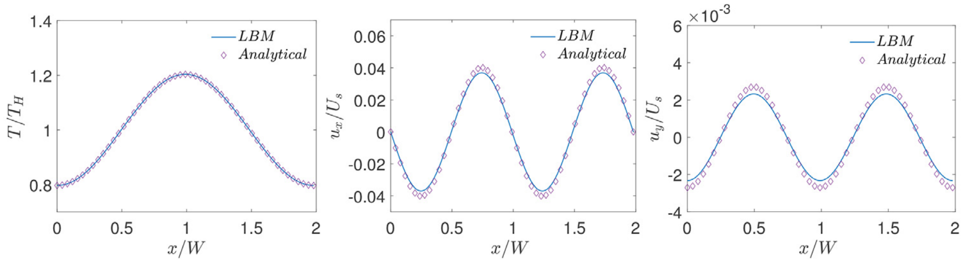

Fig. 21. Profiles of the temperature and velocity components along the centerline of the domain in the x direction for thermocapillary flow in SRFs for thermal conductivity ratio $\tilde{k} = 1.0$. The purple symbols shown are obtained from the analytical solution and the lines are the LB simulation results. Here, the aspect ratio is $a/b = 1$, viscosity ratio is $\tilde{\mu} = 1$, and the dimensionless surface tension coefficients are $M_1 = 0$ and $M_2 = 1 \times 10^{-1}$. (For interpretation of the references to color in this figure legend, the reader is referred to the web version of this article.)

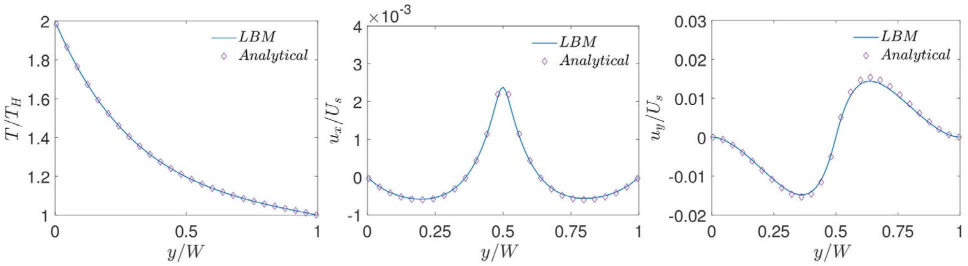

Fig. 22. Profiles of the temperature and velocity components along the centerline of the domain in the y direction for thermocapillary flow in SRFs for thermal conductivity ratio $\tilde{k} = 1.0$. The purple symbols shown are obtained from the analytical solution and the lines are the LB simulation results. Here, the aspect ratio is $a/b = 1$, viscosity ratio is $\tilde{\mu} = 1$, and the dimensionless surface tension coefficients are $M_1 = 0$ and $M_2 = 1 \times 10^{-1}$. (For interpretation of the references to color in this figure legend, the reader is referred to the web version of this article.)

in SRFs based on our new analytical solution derived earlier are in good quantitative agreement with the numerical results based on the central moment LB schemes constructed in the previous sections.

6.4. *Effect of characteristic parameters on peak interfacial thermocapillary velocity $U_{\max}$ in SRF layers*

Let's now study the effect of various dimensionless variables on the magnitude of the peak velocity generated on the interface $U_{\max}$, as a global parameter indicating the strength of the thermo-

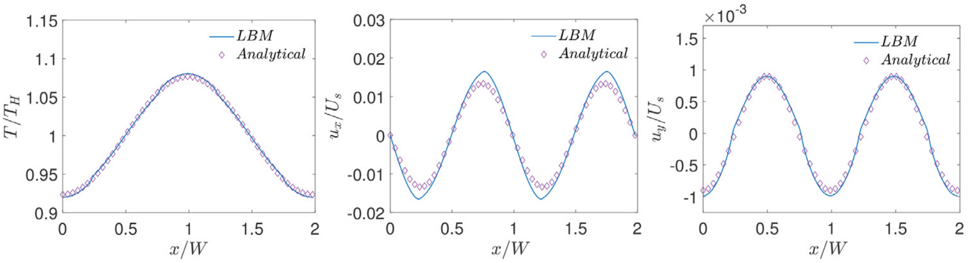

Fig. 23. Profiles of the temperature and velocity components along the centerline of the domain in the x direction for thermocapillary flow in SRFs for thermal conductivity ratio $\tilde{k} = 5.0$. The purple symbols shown are obtained from the analytical solution and the lines are the LB simulation results. Here, the aspect ratio is $a/b = 1$, viscosity ratio is $\tilde{\mu} = 1$, and the dimensionless surface tension coefficients are $M_1 = 0$ and $M_2 = 1 \times 10^{-1}$. (For interpretation of the references to color in this figure legend, the reader is referred to the web version of this article.)

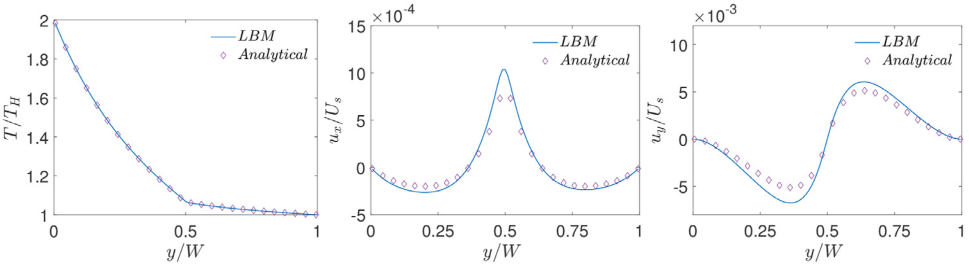

Fig. 24. Profiles of the temperature and velocity components along the centerline of the domain in the y direction for thermocapillary flow in SRFs for thermal conductivity ratio $\tilde{k} = 5.0$. The purple symbols shown are obtained from the analytical solution and the lines are the LB simulation results. Here, the aspect ratio is $a/b = 1$, viscosity ratio is $\tilde{\mu} = 1$, and the dimensionless surface tension coefficients are $M_1 = 0$ and $M_2 = 1 \times 10^{-1}$. (For interpretation of the references to color in this figure legend, the reader is referred to the web version of this article.)

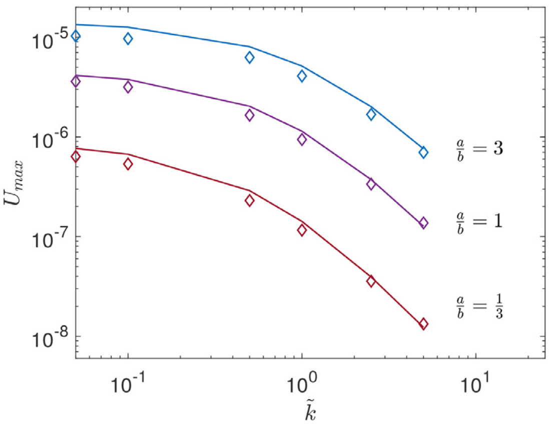

Fig. 25. Effect of the thermal conductivity ratio $\tilde{k}$ on the maximum thermocapillary velocity at the interface in SRFs for three different values of the aspect ratio a/b. The results from the analytical solution are shown as lines and LBM results are shown as symbols. Here, the viscosity ratio is $\tilde{\mu} = 1$, the dimensionless surface tension coefficients are $M_1 = 0$ and $M_2 = 5 \times 10^{-2}$, and $\sigma_0 = 1 \times 10^{-3}$.

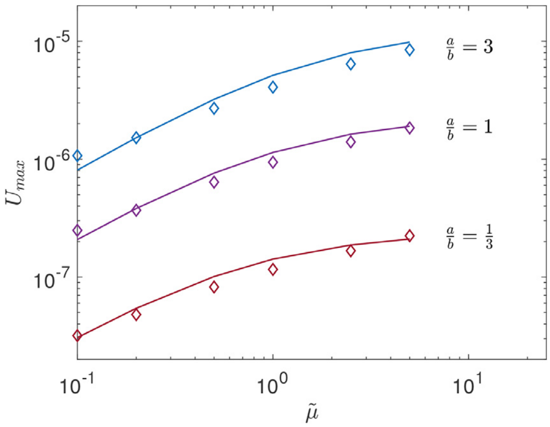

Fig. 26. Effect of the viscosity ratio $\tilde{\mu}$ on the maximum thermocapillary velocity at the interface in SRFs for three different values of the aspect ratio a/b. The results from the analytical solution are shown as lines and LBM results are shown as symbols. Here, the thermal conductivity ratio is $\tilde{k} = 1$, the dimensionless surface tension coefficients are $M_1 = 0$ and $M_2 = 5 \times 10^{-2}$, and $\sigma_0 = 1 \times 10^{-3}$.

capillary convection in SRFs. First, we investigate the effect of the thermal conductivity ratio $\tilde{k}$ on $U_{\max}$. Figure 25 shows the variation of the dimensionless peak velocity on the interface as a function of the thermal conductivity ratio for three different choices of the aspect ratio, viz., $a/b = 1/3$, 1, and 3, when $\tilde{\mu} = 1$. For a fixed a/b, it can be observed that as the thermal conductivity ratio increases, or the top fluid layer is thermally more conducting than the bottom fluid layer, $U_{\max}$ is found to decrease monotonically; conversely, notice that the peak thermocapillary convection current can be enhanced by decreasing $\tilde{k}$ or, equivalently, by maintaining the thermal conductivity of the top fluid layer constant and increasing the thermal conductivity of the bottom fluid layer; the latter increases the heat flux from the bottom SRF layer, which results in a more pronounced nonuniform temperature distribution along the interface; in turn, greater Marangoni stresses are generated, which result in stronger fluid motions around the interfaces. In addition, it is evident from Fig. 25 that the ratio of fluid thicknesses a/b has a significant effect on $U_{\max}$. In general, for a fixed thermal conductivity ratio, when the bottom fluid layer is thinner than the top fluid layer, i.e., $a/b > 1$, their interface lies closer to the heated bottom wall, which in turn enhances thermocapillary convection due to its stronger nonuniform heating, which results in a larger peak Marangoni velocity. For example, when $\tilde{k} = 1.0$, by changing a/b from $1/3$ to 3 increases U_r by more than ten times.

Next, Fig. 26 shows the effect of the dimensionless viscosity ratio $\tilde{\mu} = \mu_a/\mu_b$ on the peak thermocapillary velocity $U_{\max}$ for $a/b = 1/3$, 1, and 3 at a fixed $\tilde{k} = 1$. Clearly, the viscosities of the SRFs have profound influence on the strength of thermocapillary

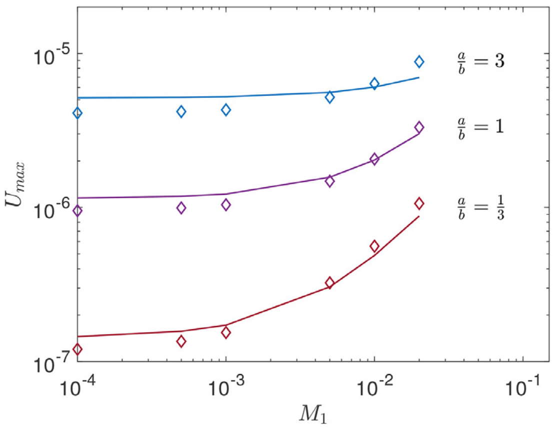

Fig. 27. Effect of the dimensionless linear coefficient of surface tension M_1 on the maximum velocity at the interface in SRFs for three different values of the aspect ratio a/b at $\tilde{k} = 1$, $\tilde{\mu} = 1$, and $M_2 = 5 \times 10^{-2}$. The results from the analytical solution are shown as lines and LBM results are shown as symbols.

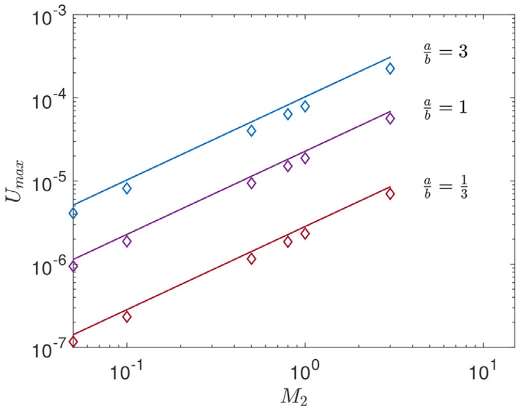

Fig. 28. Effect of the dimensionless quadratic coefficient of surface tension M_2 on the maximum velocity at the interface in SRFs for three different values of the aspect ratio a/b at $\tilde{k} = 1$, $\tilde{\mu} = 1$, and $M_1 = 1 \times 10^{-5}$. The results from the analytical solution are shown as lines and LBM results are shown as symbols.

convection. In particular, if the bottom fluid layer is less viscous than the top fluid layer, or $\tilde{\mu} > 1$, it more readily promotes the exchange of momentum transfer between the interface and the layers of the bottom fluid due to weaker flow resistance, which is then accompanied by larger peak thermocapillary velocities. Thus, the increasing the viscosity ratio has an opposite effect when compared to the thermal conductivity ratio. On the other hand, for a fixed viscosity ratio, the variations in the thickness ratio a/b has a similar influence as noticed in the previous case.

Finally, Figs. 27 and 28 present the effects of the dimensionless linear and quadratic coefficients, M_1 and M_2, respectively, on the peak thermocapillary velocity $U_{\max}$ for $a/b = 1/3$, 1, and 3 at fixed $\tilde{k} = 1$ and $\tilde{\mu} = 1$ (see Eq. (7) for their definitions based on σ_T and σ_{TT}). Evidently, increasing either M_1 or M_2 increases the strength of the Marangoni velocity. This is due to the fact that M_1 and M_2 represent the sensitivities of the surface tension on the temperature. The larger the magnitude of these parameters the greater is the surface tension gradient or the Marangoni stress on the interface, which then manifest as thermocapillary flow with higher peak velocities. Generally, such effects are more pronounced when the interface is located closer to the heated bottom wall or with increasing a/b which is consistent with the observations made earlier in Section 6.2. Interestingly, it is noted that the effect of variations in the linear surface tension coefficient M_1 on $U_{\max}$ for fixed $M_2 = 5 \times 10^{-2}$ is greater at $a/b = 1/3$ when compared to the other cases; on the other hand, for a fixed $M_1 = 1 \times 10^{-5}$, $U_{\max}$ increases in direct proportion with an increase in the quadratic coefficient M_2 with a constant slope (which is consistent with the characteristic velocity dependence on σ_{TT} or, equivalently, M_2 given in Eq. (32)) for all choices of the aspect ratio a/b.

6.5. Beyond the analytical solution: Interfacial deformations at higher capillary numbers using lattice Boltzmann simulations

In the derivation of the new analytical solution for thermocapillary convection in SRF layers, it was assumed that the interface remains flat which is a reasonable assumption at relatively small capillary numbers and applicable for microchannel configurations. It is consistent with those considered in prior work (see e.g., Pendse and Esmaeeli [10]) and, as shown in the previous section, the results obtained from such a theoretical analysis were in good quantitative agreement with the numerical simulations under similar conditions. However, it should be pointed out that the computational approach discussed in Section Appendix A is not restricted by such assumptions and is applicable for more general situations, where the interfaces between the SRFs can deform, which can arise at relatively large capillary numbers. In order to simply illustrate this viewpoint, we have performed some additional simulations involving SRF layers at progressively increasing values of the capillary number Ca while maintaining $M_1 = 0$ and $\sigma_0 = 1 \times 10^{-3}$ with $a/b = 3$ with thermal conductivity ratio $\tilde{k} = 1$ and viscosity ratio $\tilde{\mu} = 1$. We chose the interface to be closer to the heated bottom wall by fixing $a/b = 3$ so that more pronounced thermocapillary convection are generated, whose magnitudes are controlled by varying the parameter M_2 which in turn determines the characteristic velocity used in defining the capillary number.

Figure 29 shows the contours of the pressure field and the streamline patterns in SRF layers computed using the LB schemes at $\mathrm{Ca} = 0.34, 0.57, 1.15,$ and 2.29 via varying M_2 as $M_2 = 3, 5, 10,$ and 20, respectively. In the results discussed earlier where $\mathrm{Ca} < 0.1$, the interface was found to be essentially flat and both the analytical solution and the numerical simulations were consistent with each other. By contrast, according to Fig. 29, as Ca is increased to 0.34, the simulations show that the interfaces undergo relatively small deformations. As Ca is progressively increased further, the interfaces deform more significantly. These result from the differences in the pressure fields between the bottom and top SRF layers which is accompanied by local variations in the curvatures or the normal capillary forces as seen from the pressure contour plots. Clearly, larger the capillary number, the larger is the pressure differences or the greater is the interfacial deformations. Interestingly, despite such interfacial deformations, the thermocapillary flow patterns are seen to be qualitatively similar to that of the flat interface cases considered earlier in that the SRF layers are accompanied with eight counterrotating vortex cells. As such, these demonstrate the capabilities of the central moment LB schemes in computing local variations in the interfacial topologies naturally and their potential of going beyond the possible parametric space of the analytical solution in simulating thermocapillary flow in SRF layers.

Before we conclude, let us now provide some selection suggestions for SRF applications as an extension of this study. First, the surface tension variation with temperature $\sigma(T)$ obtained empirically should be curve fitted to a parabolic profile according to Eq. (4) to deduce the linear σ_T and quadratic σ_{TT} sensitivity coefficients of the surface tension on temperature. Moreover, other thermophysical properties as noted in Section 2.3 should be chosen. Then, the computational formulation discussed in Section 4 and further elaborated for computing the fluid motions, interface tracking, and the energy transport in the attendant appendices (Appendices Appendix A and Appendix B) can be used

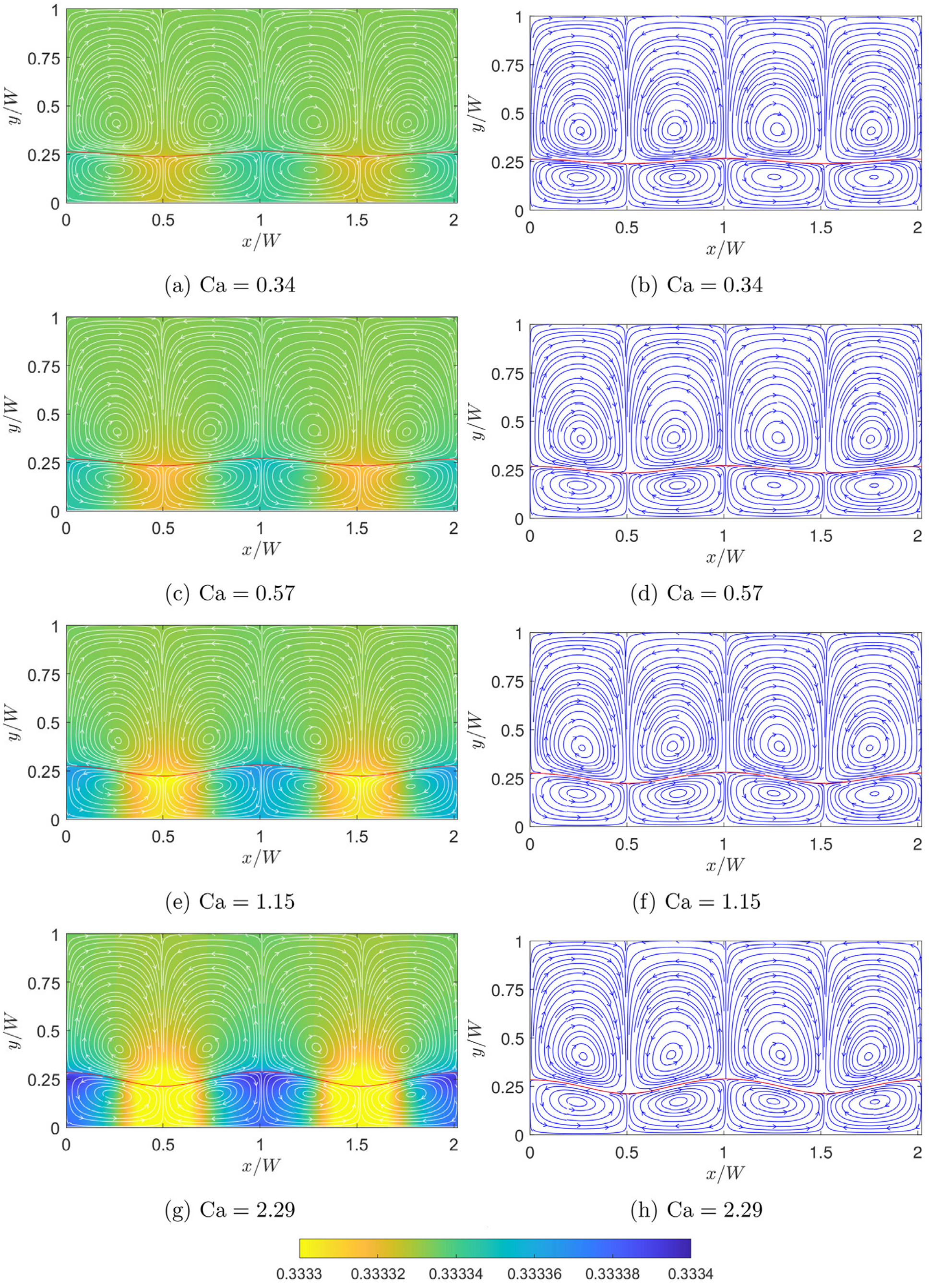

Fig. 29. Simulations of interfacial deformations using the central moment LB schemes at higher capillary numbers in SRF layers. (a) Pressure contours and (b) streamlines of the thermocapillary flow for aspect ratio $a/b = 3$ with thermal conductivity ratio $\tilde{k} = 1$ and viscosity ratio $\tilde{\mu} = 1$ at different capillary numbers Ca.

to investigate the underlying physics in a variety of SRF applications. In this regard, some selection suggestions include the thermocapillary convection of multilayer SRFs microchannels, manipulating the drop or bubble migration dynamics, and enhancement of thermal transport in heat pipes and pool boiling processes. The lattice Boltzmann formulation presented in this work is general and can be readily used to incorporate a variety of thermal and flow configurations in such SRF applications and to study the details of thermocapillary flow and mixing patterns, interfacial deformations, and the heat transfer rates.

7. Summary and conclusions

Surface tension in fluids is a temperature dependent property and is among the main drivers of interfacial transport phenomena. In contrast to the normal fluids (NFs), the self-rewetting fluids (SRFs) exhibit anomalous nonlinear (quadratic) dependence of surface tension on temperature with a minimum and involving a positive gradient. As a result, they are accompanied by certain desirable aspects, such as interfacial fluid motions towards high temperature regions, which can be potentially exploited in various microgravity and terrestrial applications, including microfluidics.

In this paper, we have derived a new analytical solution for thermocapillary convection in superimposed two SRF fluid layers confined within a microchannel that is heated on its bottom side with a sinusoidally varying temperature. The derived streamfunction from solving a biharmonic equation consists of a fundamental solution resulting from the linear part of the surface tension and a higher order harmonic solution with a wavenumber that is twice that of the former and arises from the quadratic part of the surface tension variation on the temperature. Moreover, we have also developed and validated a robust numerical technique based on central moment lattice Boltzmann (LB) schemes for interface tracking based on a conservative Allen-Cahn equation, two-fluid motion, and energy transport to simulate thermocapillary convection in SRFs.

It is found that the two SRF layers are accompanied by a set of eight, periodic counterrotating convection cells with the interfacial fluid motion directed towards the high temperature at the center; by contrast, in the two NF layers, only four periodic counterrotating vortices are generated with the fluids moving away from the center along the interface. Such striking differences are well reproduced by both our analytical and computational approaches, and they are found to be in good quantitative agreement. The presence of double the number of convection cells in SRFs when compared that in NFs can be theoretically interpreted as arising from the higher order harmonic solution as noted above. It is shown that the magnitude of the linear coefficient of the surface tension variation with temperature relative to that of the quadratic coefficient of SRFs not only affects the strength of thermocapillary velocities, but also the character of the overall convection patterns. Moreover, a study of the effect of various characteristic parameters such as the thickness ratio of the fluids, thermal conductivity ratio and the viscosity ratio on the magnitude of thermocapillary convection was performed. It is found that the thermocapillary convection currents are more intense when the interface is closer to the heated bottom wall, or if the bottom fluid layer has higher thermal conductivity or lower viscosity when compared to those in the top fluid layer. In particular, as the thickness ratio is changed from 1/3 to 3, the maximum thermocapillary velocity is found to increase by about an order of magnitude; moreover, the latter is found to double as the dimensionless quadratic surface tension sensitivity coefficient increases by a factor of 2. By going beyond the analytical solution regime, computations show that at relatively larger capillary numbers the interfaces undergo deformation while maintaining the general flow patterns in SRFs as noted above. Since both our analytical and computational approaches are developed and utilized based on a general parabolic equation of state for surface tension containing the linear and quadratic terms, the results of this work are readily applicable to various SRF formulations.

The analytical solution for thermocapillary convection in SRFs derived in this work is useful not only in clarifying the essential transport physics involved, including its ability to predict the doubling of the number of vortex cells in SRFs when compared to that in NFs, but may also serve as a benchmark solution in constructing new numerical techniques for simulating thermocapillary flows in SRFs. The central moment LB schemes are not only quantitatively in agreement with such a solution, but provides an approach to extend it to more general situations involving interfacial deformations. The ability to modulate both the surface-tension driven flow patterns and their magnitudes in SRFs in certain unique manner relative to NFs, such as those shown in this work, could provide new approaches in manipulating interfacial transport phenomena in microfluidic applications.

Declaration of Competing Interest

The authors declare that they have no known competing financial interests or personal relationships that could have appeared to influence the work reported in this paper.

CRediT authorship contribution statement

Bashir Elbousefi: Data curation, Formal analysis, Investigation, Methodology, Software, Visualization, Writing – original draft. **William Schupbach:** Data curation, Formal analysis, Investigation, Methodology, Software, Visualization, Writing – original draft. **Kannan N. Premnath:** Conceptualization, Formal analysis, Funding acquisition, Investigation, Methodology, Supervision, Writing – review & editing. **Samuel W.J. Welch:** Methodology, Supervision, Writing – review & editing.

Data availability

Data will be made available on request.

Acknowledgments

The authors would like to acknowledge the support of the US National Science Foundation (NSF) for research under Grant CBET-1705630. The third author (KNP) would also like to thank the NSF for support of the development of a computer cluster ‘Alderaan’ hosted at the Center for Computational Mathematics at the University of Colorado Denver under Grant OAC-2019089 (Project “CC* Compute: Accelerating Science and Education by Campus and Grid Computing”), which was used in performing the simulations.

Appendix A. Numerical algorithms: central moment lattice Boltzmann schemes for interface tracking, two-fluid motion and energy transport

In this section, we will present a numerical LB approach based on more robust collision models involving central moments [49,50,52,64] for solving the equations of the phase-field model for tracking the interface (Eq. (24)) and the binary fluid motions (Eqs. (25)–(28)) given in the previous section, along with the transport of energy presented in Eq. (3c) earlier. Solving these three equations requires evolving three separate distribution functions on the standard two-dimensional, square lattice (D2Q9) lattice, which involve performing a *collision step* based on the relaxation of different central moments of the distribution function to their equilibria, which is followed by a lock-step advection of the distribution functions to their adjacent nodes along the characteristic directions in the *streaming step*. Then, the macroscopic variables, viz., the order parameter, the fluid pressure and velocity, as well as the temperature field, are obtained via taking the moments of the respective distribution functions. It should be noted that since the collision step is performed using central moments while the streaming step is performed by means of the distribution functions, this requires the use of appropriate mappings that transform between these quantities pre- and post-collision step. The central moment LB methods are shown to be more robust (e.g., enhanced numerical stability) when compared to the other collision models in the LB framework (see Hajabdollahi et al. [50], Yahia and Premnath [65], Yahia et al. [66] for recent examples). While the recent central moment LB scheme for two-fluid interfacial flows [50] was constructed using an orthogonal moment basis, in what follows, we will present an improved formulation involving the non-orthogonal moment basis.

A1. LB scheme for phase-field based interface capturing

We will now discuss a central moment LB technique to solve the conservative ACE given in Eq. (24) by evolving a distribution function f_α, where $\alpha = 0, 1, 2, \ldots, 8$ represent the discrete particle directions, on the D2Q9 lattice. Generally, during collision, the set of distribution functions $\mathbf{f} = (f_0, f_1, f_2, \ldots, f_8)^\dagger$ relax to the corresponding equilibrium distribution functions given by $\mathbf{f}^{eq} = (f_0^{eq}, f_1^{eq}, f_2^{eq}, \ldots, f_8^{eq})^\dagger$, which needs to be implement via their central moments in what follows.

In this regard, first, the components of the particle velocities of this lattice can be represented by the following vectors in standard Dirac's bra-ket notation as

$$|\boldsymbol{e}_x\rangle = (0, 1, 0, -1, 0, 1, -1, -1, 0)^\dagger,$$
$$|\boldsymbol{e}_y\rangle = (0, 0, 1, 0, -1, 1, 1, -1, -1)^\dagger.$$

We also need the following 9-dimensional vector to define the zeroth moment of f_α:

$$|\mathbf{1}\rangle = (1, 1, 1, 1, 1, 1, 1, 1, 1)^\dagger.$$

That is, its inner product with the set of distribution functions $\langle \mathbf{f}|\mathbf{1}\rangle$ should yield the order parameter ϕ of the phase-field model. The central moment LB will then be constructed based on the following set of nine non-orthogonal basis vectors (which differs from the approach presented in Hajabdollahi et al. [50]):

$$|P_0\rangle = |\mathbf{1}\rangle, \quad |P_1\rangle = |\boldsymbol{e}_x\rangle, \quad |P_2\rangle = |\boldsymbol{e}_y\rangle,$$
$$|P_3\rangle = \left|\boldsymbol{e}_x^2 + \boldsymbol{e}_y^2\right\rangle, \quad |P_4\rangle = \left|\boldsymbol{e}_x^2 - \boldsymbol{e}_y^2\right\rangle, \quad |P_5\rangle = |\boldsymbol{e}_x\boldsymbol{e}_y\rangle,$$
$$|P_6\rangle = \left|\boldsymbol{e}_x^2\boldsymbol{e}_y\right\rangle, \quad |P_7\rangle = \left|\boldsymbol{e}_x\boldsymbol{e}_y^2\right\rangle, \quad |P_8\rangle = \left|\boldsymbol{e}_x^2\boldsymbol{e}_y^2\right\rangle.$$

Symbols like $\left|e_x^2 e_y\right\rangle = |e_x e_x e_y\rangle$ signify a vector that results from the element-wise vector multiplication of vectors $|e_x\rangle, |e_x\rangle$ and $|e_y\rangle$. They can be grouped together in the form of the following matrix that maps the distribution functions to the *raw* moments in terms of the above moment basis vectors:

$$\mathbf{P} = [\langle P_0|, \langle P_1|, \langle P_2|, \langle P_3|, \langle P_4|, \langle P_5|, \langle P_6|, \langle P_7|, \langle P_8|\,]. \tag{34}$$

Here, it should be noted that the *central* moments are obtained from the distribution moments by shifting the particle velocity $\boldsymbol{e}_\alpha$ by the fluid velocity $\boldsymbol{u}$. Given these, we can then formally define the raw moments of the distribution function f_α as well as its equilibrium f_α^{eq} as

$$\begin{pmatrix} \kappa'_{mn} \\ \kappa'^{\,eq}_{mn} \end{pmatrix} = \sum_{\alpha=0}^{8} \begin{pmatrix} f_\alpha \\ f_\alpha^{eq} \end{pmatrix} e_{\alpha x}^m e_{\alpha y}^n, \tag{35a}$$

and the corresponding central moments as

$$\begin{pmatrix} \kappa_{mn} \\ \kappa^{eq}_{mn} \end{pmatrix} = \sum_{\alpha=0}^{8} \begin{pmatrix} f_\alpha \\ f_\alpha^{eq} \end{pmatrix} (e_{\alpha x} - u_x)^m (e_{\alpha y} - u_y)^n. \tag{35b}$$

Thus, κ'_{mn} represents the raw moment of order $(m+n)$, while the corresponding central moment is κ_{mn}. For convenience, we can group all the possible raw moments and the central moments for the D2Q9 lattice via the following two vectors as

$$\boldsymbol{\kappa}' = (\kappa'_{00}, \kappa'_{10}, \kappa'_{01}, \kappa'_{20}, \kappa'_{02}, \kappa'_{11}, \kappa'_{21}, \kappa'_{12}, \kappa'_{22}), \tag{36a}$$

$$\boldsymbol{\kappa} = (\kappa_{00}, \kappa_{10}, \kappa_{01}, \kappa_{20}, \kappa_{02}, \kappa_{11}, \kappa_{21}, \kappa_{12}, \kappa_{22}). \tag{36b}$$

It should be noted that one can readily map from the distribution functions to the raw moments via $\boldsymbol{\kappa}' = \mathbf{P}\mathbf{f}$, which can then be transformed into the central moments through $\boldsymbol{\kappa} = \mathsf{F}\boldsymbol{\kappa}'$, where the F follows readily from binomial expansions of $(e_{\alpha x} - u_x)^m (e_{\alpha y} - u_y)^n$ to relate to $e_{\alpha x}^m e_{\alpha y}^n$ etc. Similarly, the inverse mappings from central moments to raw moments, from which the distribution functions can be recovered via the matrices F^{-1} and P^{-1}, respectively. All these mapping relations are explicitly listed in Appendix B.

As mentioned above, a key aspect of our approach is to perform the collision step such that different central moments shown above relax to their corresponding central moment equilibria. The discrete central moment equilibria κ_{mn}^{eq} defined above can be obtained by matching them to the corresponding central moments of the continuous Maxwell distribution function after replacing the density ρ with the order parameter ϕ; furthermore, the interface sharpening flux terms in the conservative ACE (Eq. (24)) need to be accounted for by augmenting the first order central moment equilibrium components with $M_\phi \theta n_x$ and $M_\phi \theta n_y$ [50]. Thus, we have

$$\kappa_{00}^{eq} = \phi, \qquad \kappa_{10}^{eq} = M_\phi \theta n_x, \qquad \kappa_{01}^{eq} = M_\phi \theta n_y,$$
$$\kappa_{20}^{eq} = c_{s\phi}^2 \phi, \qquad \kappa_{02}^{eq} = c_{s\phi}^2 \phi, \qquad \kappa_{11}^{eq} = 0,$$
$$\kappa_{21}^{eq} = 0, \qquad \kappa_{12}^{eq} = 0, \qquad \kappa_{22}^{eq} = c_{s\phi}^4 \phi, \tag{37}$$

where $c_{s\phi}^2 = 1/3$.

Based on the above considerations, inspired from the algorithmic implementation presented in Geier et al. [67] (see also [65,66]), we can now summarize the central moment LB algorithm for solving the conservative ACE for a time step Δt starting from $f_\alpha = f_\alpha(\boldsymbol{x}, t)$ as follows:

- Compute pre-collision raw moments from distribution functions via $\boldsymbol{\kappa}' = \mathbf{P}\mathbf{f}$ (see Eq. (51) in Appendix B for $\mathbf{P}$)
- Compute pre-collision central moments from raw moments via $\boldsymbol{\kappa} = \mathsf{F}\boldsymbol{\kappa}'$ (see Eq. (52) in Appendix B for F)
- Perform collision step via relaxation of central moments κ_{mn} to their equilibria κ_{mn}^{eq}:
$$\tilde{\kappa}_{mn} = \kappa_{mn} + \omega_{mn}^\phi (\kappa_{mn}^{eq} - \kappa_{mn}), \tag{38}$$
where $(mn) = (00), (10), (01), (20), (02), (11), (21), (12)$, and (22), and ω_{mn}^ϕ is the relaxation parameter for moment of order $(m+n)$. Here, the implicit summation convention of repeated indices is not assumed. The relaxation parameters of the first order moments $\omega_{10}^\phi = \omega_{01}^\phi = \omega^\phi$ are related to the mobility coefficient M_ϕ in Eq. (24) via $M_\phi = c_{s\phi}^2\left(\frac{1}{\omega^\phi} - \frac{1}{2}\right)\Delta t$, and the rest of the relaxation parameters are typically set to unity, i.e., $\omega_{mn}^\phi = 1.0$, where $(m+n) \geq 2$. The results of Eq. (38) are then grouped in $\tilde{\boldsymbol{\kappa}}$.
- Compute post-collision raw moments from post-collision central moments via $\tilde{\boldsymbol{\kappa}}' = \mathsf{F}^{-1}\tilde{\boldsymbol{\kappa}}$ (see Eq. (53) in Appendix B for F^{-1})
- Compute post-collision distribution functions from post-collision raw moments via $\tilde{\mathbf{f}} = \mathsf{P}^{-1}\tilde{\boldsymbol{\kappa}}'$ (see Eq. (54) in Appendix B for P^{-1})
- Perform streaming step via $f_\alpha(\boldsymbol{x}, t+\Delta t) = \tilde{f}_\alpha(\boldsymbol{x} - \boldsymbol{e}_\alpha \Delta t)$, where $\alpha = 0, 1, 2, \ldots, 8$.
- Update the order parameter ϕ of the phase-field model for interface capturing through
$$\phi = \sum_{\alpha=0}^{8} f_\alpha. \tag{39}$$

A2. LB scheme for two-fluid motion with capillary and Marangoni forces

Next, we will present a central moment LB scheme to solve the motion of binary fluids with interfacial forces represented in

Eqs. (25)–(28) by evolving another distribution function g_α, where $\alpha = 0, 1, 2, \ldots, 8$. Our approach is based on a discretization of the modified continuous Boltzmann equation and obtaining the discrete central moment equilibria and central moments of the source terms for the body forces via a matching principle with their continuous counterparts as detailed in Ref. [50]. However, in contrast to Ref. [50], where an orthogonal moment basis is employed resulting in the so-called cascaded LB approach, in the following, we consider the simpler, non-orthogonal moment basis vectors as given earlier in Eq. (34).

As in the previous section, we first define the following raw moments and the central moments of the distribution function g_α, its equilibrium g_α^{eq}, as well as the source term S_α, where the latter accounts for the surface tension and body forces, as well as those that arising from the application of a transformation to simulate flows at high density ratios in the incompressible limit (see He et al. [46], Hajabdollahi et al. [50]):

$$\begin{pmatrix} \eta'_{mn} \\ \eta'^{\,eq}_{mn} \\ \sigma'_{mn} \end{pmatrix} = \sum_{\alpha=0}^{8} \begin{pmatrix} g_\alpha \\ g_\alpha^{eq} \\ S_\alpha \end{pmatrix} e^m_{\alpha x} e^n_{\alpha y}, \tag{40a}$$

$$\begin{pmatrix} \eta_{mn} \\ \eta^{eq}_{mn} \\ \sigma_{mn} \end{pmatrix} = \sum_{\alpha=0}^{8} \begin{pmatrix} g_\alpha \\ g_\alpha^{eq} \\ S_\alpha \end{pmatrix} (e_{\alpha x} - u_x)^m (e_{\alpha y} - u_y)^n. \tag{40b}$$

For conveniences, we can group the elements of the distribution function, its equilibrium, and the source term for the D2Q9 lattice as the following vectors: $\mathbf{g} = (g_0, g_1, g_2, \ldots, g_8)^\dagger$, $\mathbf{g}^{eq} = (g_0^{eq}, g_1^{eq}, g_2^{eq}, \ldots, g_8^{eq})^\dagger$, and $\mathbf{S} = (S_0, S_1, S_2, \ldots, S_8)^\dagger$. Moreover, we group all the possible raw moments and the central moments defined above for the D2Q9 lattice via the following:

$$\boldsymbol{\eta}' = (\eta'_{00}, \eta'_{10}, \eta'_{01}, \eta'_{20}, \eta'_{02}, \eta'_{11}, \eta'_{21}, \eta'_{12}, \eta'_{22}), \tag{41a}$$

$$\boldsymbol{\eta} = (\eta_{00}, \eta_{10}, \eta_{01}, \eta_{20}, \eta_{02}, \eta_{11}, \eta_{21}, \eta_{12}, \eta_{22}), \tag{41b}$$

and similarly for raw moments and the central moments the equilibrium and the source term.

The collision step will be performed such that different central moments shown above relax to their corresponding central moment equilibria, which are augmented by changes in the central moments due to the net forces; the latter is given by sum the surface tension force $\boldsymbol{F}_s = (F_{sx}, F_{sy})$, which can have contributions from both the capillary and Marangoni forces as represented in Eq. (28), and any external force $\boldsymbol{F}_{ext} = (F_{ext,x}, F_{ext,y})$, i.e., $\boldsymbol{F}_t = \boldsymbol{F}_s + \boldsymbol{F}_{ext}$ or $(F_{tx}, F_{ty}) = (F_{sx} + F_{ext,x}, F_{sy} + F_{ext,y})$. Moreover, the use of an incompressible transformation as mentioned above leads to a pressure-based formulation, involving the incorporation of a net pressure force $\boldsymbol{F}_p$ arising from $\varphi(\rho) = p - \rho c_s^2$, i.e., $\boldsymbol{F}_p = -\nabla\varphi$, or $(F_{px}, F_{py}) = (-\partial_x\varphi, -\partial_y\varphi)$ (see Hajabdollahi et al. [50] for details). Then, the discrete central moment equilibria η_{mn} defined above can be obtained by matching them to the corresponding continuous central moments of the equilibrium that arise from the incompressible transformation, and similarly for the central moments of the source term σ_{mn}, which then results in the following expressions for the D2Q9 lattice [50]:

$$\begin{aligned} \eta^{eq}_{00} &= p, \quad \eta^{eq}_{10} = -\varphi(\rho)u_x, \quad \eta^{eq}_{01} = -\varphi(\rho)u_y, \\ \eta^{eq}_{20} &= pc_s^2 + \varphi(\rho)u_x^2, \quad \eta^{eq}_{02} = pc_s^2 + \varphi(\rho)u_y^2, \quad \eta^{eq}_{11} = \varphi(\rho)u_x u_y, \\ \eta^{eq}_{21} &= -\varphi(\rho)(u_x^2 + c_s^2)u_y, \quad \eta^{eq}_{12} = -\varphi(\rho)(u_y^2 + c_s^2)u_x, \\ \eta^{eq}_{22} &= c_s^6\rho + \varphi(\rho)(u_x^2 + c_s^2)(u_y^2 + c_s^2). \end{aligned} \tag{42}$$

and

$$\begin{aligned} \sigma_{00} &= \Gamma^p_{00}, \quad \sigma_{10} = c_s^2 F_{tx} - u_x\Gamma^p_{00}, \\ \sigma_{01} &= c_s^2 F_{ty} - u_y\Gamma^p_{00}, \\ \sigma_{20} &= 2c_s^2 F_{px}u_x + (u_x^2 + c_s^2)\Gamma^p_{00}, \\ \sigma_{02} &= 2c_s^2 F_{py}u_y + (u_y^2 + c_s^2)\Gamma^p_{00}, \\ \sigma_{11} &= c_s^2(F_{px}u_y + F_{py}u_x) + u_x u_y\Gamma^p_{00}, \quad \sigma_{21} = 0, \\ \sigma_{12} &= 0, \quad \sigma_{22} = 0, \end{aligned} \tag{43}$$

where $\Gamma^p_{00} = (F_{px}u_x + F_{py}u_y)$.

Using the above developments, we can now summarize the central moment LB algorithm for computing the two-fluid motion with interfacial forces for a time step Δt starting from $g_\alpha = g_\alpha(\boldsymbol{x}, t)$ as follows:

- Compute pre-collision raw moments from distribution functions via $\boldsymbol{\eta}' = \mathbf{P}\mathbf{g}$ (see Eq. (51) in Appendix B for $\mathbf{P}$)
- Compute pre-collision central moments from raw moments via $\boldsymbol{\eta} = \mathbf{F}\boldsymbol{\eta}'$ (see Eq. (52) in Appendix B for $\mathbf{F}$)
- Perform collision step via relaxation of central moments η_{mn} to their equilibria η^{eq}_{mn} and augmented with the source terms σ_{mn}: In order to allow for an independent specification of the shear viscosity ν from the bulk viscosity ζ, the trace of the second order moments $\eta_{20} + \eta_{02}$ should be evolved independently from the other second order moments. To accomplish this, prior to collision, we combine the diagonal parts of the second order moments as follows (see e.g., Yahia and Premnath [65], Yahia et al. [66], Geier et al. [67]):

  $$\eta_{2s} = \eta_{20} + \eta_{02}, \qquad \eta^{eg}_{2s} = \eta^{eg}_{20s} + \eta^{eg}_{02}, \qquad \sigma_{2s} = \sigma_{20s} + \sigma_{02},$$

  $$\eta_{2d} = \eta_{20} - \eta_{02}, \qquad \eta^{eg}_{2d} = \eta^{eg}_{20s} - \eta^{eg}_{02}, \qquad \sigma_{2d} = \sigma_{20s} - \sigma_{02},$$

  and thus η_{2s} and η_{2d} will be evolved independently under collision. Then, the post-collision central moments under relaxation and augmentation due to the forces can be computed via

  $$\tilde{\eta}_{mn} = \eta_{mn} + \omega_{mn}\left(\eta^{eq}_{mn} - \eta_{mn}\right) + (1 - \omega_{mn}/2)\sigma_{mn}\Delta t, \tag{44}$$

  where ω_{mn} is the relaxation time corresponding to the central moment η_{mn}, and $(mn) = (00), (10), (01), (2s), (2d), (11), (21), (12), \text{and}, (22)$. Here, the relaxation parameter ω_{2s} is related to the bulk viscosity via $\zeta = c_s^2(1/\omega_{2s} - 1/2)\Delta t$, while the relaxation parameters ω_{2d} and ω_{11} are related to the shear viscosity via $\nu = c_s^2\left(1/\omega_{ij} - 1/2\right)\Delta t$ where $(ij) = (2d), (11)$. Typically, $c_s^2 = 1/3$. In view of Eq. (29) it should be noted that if the bulk fluid properties are different, the relaxation parameters ω_{2d} and ω_{11} will then vary locally across the interface. The rest of the relaxation parameters of central moments are generally set to unity, i.e., $\omega_{ij} = 1.0$, where $(ij) = (00), (10), (01), (2s), (21), (12), (22)$. Also, the combined forms of the post-collision central moments $\tilde{\eta}_{2s}$ and $\tilde{\eta}_{2d}$ are then segregated in their individual components $\tilde{\eta}_{20}$ and $\tilde{\eta}_{02}$ via

  $$\tilde{\eta}_{20} = \frac{1}{2}(\tilde{\eta}_{2s} + \tilde{\eta}_{2d}), \qquad \tilde{\eta}_{02} = \frac{1}{2}(\tilde{\eta}_{2s} - \tilde{\eta}_{2d}).$$

  Finally, the results of Eq. (44) by accounting for the above segregation are then grouped in $\tilde{\boldsymbol{\eta}}$.
- Compute post-collision raw moments from post-collision central moments via $\tilde{\boldsymbol{\eta}}' = \mathbf{F}^{-1}\tilde{\boldsymbol{\eta}}$ (see Eq. (53) in Appendix B for $\mathbf{F}^{-1}$)
- Compute post-collision distribution functions from post-collision raw moments via $\tilde{\mathbf{g}} = \mathbf{P}^{-1}\tilde{\boldsymbol{\eta}}'$ (see Eq. (54) in Appendix B for $\mathbf{P}^{-1}$)
- Perform streaming step via $g_\alpha(\boldsymbol{x}, t + \Delta t) = \tilde{g}_\alpha(\boldsymbol{x} - \boldsymbol{e}_\alpha\Delta t)$, where $\alpha = 0, 1, 2, \ldots, 8$.

- Update the pressure field p and the components of the fluid velocity $\boldsymbol{u}=(u_x,u_y)$ through

$$p=\sum_\alpha g_\alpha+\frac{1}{2}\boldsymbol{F}_p\cdot\boldsymbol{u}\Delta t,\quad \rho c_s^2\boldsymbol{u}=\sum_\alpha g_\alpha\boldsymbol{e}_\alpha+\frac{1}{2}c_s^2\boldsymbol{F}_t\Delta t. \tag{45}$$

A3. LB scheme for energy equation

Finally, we will now discuss a central moment LB approach for the solution of the energy transport equation (Eq. (3c)) by evolving a third distribution function h_α, where $\alpha=0,1,2,\ldots,8$, on the D2Q9 lattice. Since Eq. (3c) is an advection-diffusion equation, its construction procedure is quite similar to that of the LB scheme for the conservative ACE presented earlier, albeit without the presence of a term such as the interface sharpening flux term which appears in the latter case. As before, we first define the following raw moments and central moments, respectively, of the distribution function h_α, as well as its equilibrium h_α^{eq}:

$$\begin{pmatrix}\chi'_{mn}\\ \chi'^{\,eq}_{mn}\end{pmatrix}=\sum_{\alpha=0}^{8}\begin{pmatrix}h_\alpha\\ h_\alpha^{eq}\end{pmatrix}e_{\alpha x}^m e_{\alpha y}^n, \tag{46a}$$

$$\begin{pmatrix}\chi_{mn}\\ \chi^{eq}_{mn}\end{pmatrix}=\sum_{\alpha=0}^{8}\begin{pmatrix}h_\alpha\\ h_\alpha^{eq}\end{pmatrix}(e_{\alpha x}-u_x)^m(e_{\alpha y}-u_y)^n. \tag{46b}$$

For convenience, we list the components of the distribution function and its equilibrium, respectively, using $\mathbf{h}=(h_0,h_1,h_2,\ldots,h_8)^\dagger$ and $\mathbf{h}^{eq}=(h_0^{eq},h_1^{eq},h_2^{eq},\ldots,h_8^{eq})^\dagger$, and analogously for the raw moments and central moments via

$$\boldsymbol{\chi}'=(\chi'_{00},\chi'_{10},\chi'_{01},\chi'_{20},\chi'_{02},\chi'_{11},\chi'_{21},\chi'_{12},\chi'_{22}), \tag{47a}$$

$$\boldsymbol{\chi}=(\chi_{00},\chi_{10},\chi_{01},\chi_{20},\chi_{02},\chi_{11},\chi_{21},\chi_{12},\chi_{22}). \tag{47b}$$

To construct a central moment-based collision model for solving the energy equation, similar to Section A.1, we obtain the discrete equilibrium central moments from the corresponding continuous counterpart of the Maxwellian by replacing the density ρ with the temperature T, and the results read as

$$\begin{aligned}&\chi_{00}^{eq}=T,\qquad \chi_{10}^{eq}=0,\qquad \chi_{01}^{eq}=0,\\ &\chi_{20}^{eq}=c_{sT}^2T,\qquad \chi_{02}^{eq}=c_{sT}^2T,\qquad \chi_{11}^{eq}=0,\\ &\chi_{21}=0,\qquad \chi_{12}^{eq}=0,\qquad \chi_{22}^{eq}=c_{sT}^4T,\end{aligned} \tag{48}$$

where, typically, $c_{sT}^2=1/3$. Then, the computational procedure for solving the energy equation for a time step Δt starting from $h_\alpha=h_\alpha(\boldsymbol{x},t)$ can be summarized as follows:

- Compute pre-collision raw moments from distribution functions via $\boldsymbol{\chi}'=\mathbf{P}\mathbf{h}$ (see Eq. (51) in Appendix B for $\mathbf{P}$)
- Compute pre-collision central moments from raw moments via $\boldsymbol{\chi}=\mathbf{F}\boldsymbol{\chi}'$ (see Eq. (52) in Appendix B for $\mathbf{F}$)
- Perform collision step via relaxation of central moments χ_{mn} to their equilibria χ_{mn}^{eq}:

$$\tilde{\chi}_{mn}=\chi_{mn}+\omega_{mn}^T(\chi_{mn}^{eq}-\chi_{mn}), \tag{49}$$

  where $(mn)=(00),(10),(01),(20),(02),(11),(21),(12),$ and (22), and ω_{mn}^T is the relaxation parameter for moment of order $(m+n)$. The relaxation parameters of the first order moments $\omega_{10}^T=\omega_{01}^T=\omega^T$ are related to the thermal diffusivity $\alpha=k/(\rho c_p)$ via $\alpha=c_{sT}^2\big(1/\omega^T-1/2\big)\Delta t$, and the rest of the relaxation parameters of higher central moments are typically set to unity. The results of Eq. (49) are then grouped in $\tilde{\boldsymbol{\chi}}$.
- Compute post-collision raw moments from post-collision central moments via $\tilde{\boldsymbol{\chi}}'=\mathbf{F}^{-1}\tilde{\boldsymbol{\chi}}$ (see Eq. (53) in Appendix B for $\mathbf{F}^{-1}$)
- Compute post-collision distribution functions from post-collision raw moments via $\tilde{\mathbf{h}}=\mathbf{P}^{-1}\tilde{\boldsymbol{\chi}}'$ (see Eq. (54) in Appendix B for $\mathbf{P}^{-1}$)
- Perform streaming step via $h_\alpha(\boldsymbol{x},t+\Delta t)=\tilde{h}_\alpha(\boldsymbol{x}-\boldsymbol{e}_\alpha\Delta t)$, where $\alpha=0,1,2,\ldots,8$.
- Update the temperature field T is obtained from

$$T=\sum_{\alpha=0}^{8}h_\alpha. \tag{50}$$

While the central moment LB schemes outlined here are applicable for a general class surface-tension driven flows with thermocapillary effects, in this work, they will be mainly applied, in conjunction with the analytical solution derived earlier, to study the effect of various characteristic parameters on the flow patterns and the intensity of thermocapillary convention in superimposed layers of two self-rewetting fluids (SRFs) bounded within a microchannel nonuniformly heated on one side.

Appendix B. Mapping relations for the central moment LB scheme on a D2Q9 lattice

Here, we summarize the various mapping relations that are needed prior to and following the collision step, where different central moments are relaxed to their equilibria, in the central moment LB scheme on the D2Q9 lattice.

The transformation matrix $\mathbf{P}$ mapping a vector of distribution functions $\mathbf{f}$ to a vector of raw moments $\boldsymbol{\kappa}'$ is given by

$$\mathbf{P}=\begin{bmatrix}1&1&1&1&1&1&1&1&1\\0&1&0&-1&0&1&-1&-1&1\\0&0&1&0&-1&1&1&-1&-1\\0&1&0&1&0&1&1&1&1\\0&0&1&0&1&1&1&1&1\\0&0&0&0&0&1&-1&1&-1\\0&0&0&0&0&1&1&-1&-1\\0&0&0&0&0&1&-1&-1&1\\0&0&0&0&0&1&1&1&1\end{bmatrix} \tag{51}$$

Next, the transformation matrix $\mathbf{F}$ mapping a vector of raw moments $\boldsymbol{\kappa}'$ to a vector of central moments $\boldsymbol{\kappa}$ reads as

$$\mathbf{F}=\begin{bmatrix}1&0&0&0&0&0&0&0&0\\-u_x&1&0&0&0&0&0&0&0\\-u_y&0&1&0&0&0&0&0&0\\u_x^2&-2u_x&0&1&0&0&0&0&0\\u_y^2&0&-2u_y&0&1&0&0&0&0\\u_xu_y&-u_y&-u_x&0&0&1&0&0&0\\-u_x^2u_y&2u_xu_y&u_x^2&-u_y&0&-2u_x&1&0&0\\-u_xu_y^2&u_y^2&2u_xu_y&0&-u_x&-2u_y&0&1&0\\u_x^2u_y^2&-u_xu_y^2&-u_x^2u_y&u_y^2&u_x^2&4u_xu_y&-2u_y&-2u_x&1\end{bmatrix} \tag{52}$$

Then, the transformation matrix $\mathbf{F}^{-1}$ mapping a vector of (post-collision) central moments $\tilde{\boldsymbol{\kappa}}$ to a vector of (post-collision) raw moments $\tilde{\boldsymbol{\kappa}}'$ can be written as

$$\mathbf{F}^{-1}=\begin{bmatrix} 1 & 0 & 0 & 0 & 0 & 0 & 0 & 0 & 0\\ u_x & 1 & 0 & 0 & 0 & 0 & 0 & 0 & 0\\ u_y & 0 & 1 & 0 & 0 & 0 & 0 & 0 & 0\\ u_x^2 & 2u_x & 0 & 1 & 0 & 0 & 0 & 0 & 0\\ u_y^2 & 0 & 2u_y & 0 & 1 & 0 & 0 & 0 & 0\\ u_xu_y & u_y & u_x & 0 & 0 & 1 & 0 & 0 & 0\\ u_x^2u_y & 2u_xu_y & u_x^2 & u_y & 0 & 2u_x & 1 & 0 & 0\\ u_xu_y^2 & u_y^2 & 2u_xu_y & 0 & u_x & 2u_y & 0 & 1 & 0\\ u_x^2u_y^2 & u_xu_y^2 & u_x^2u_y & u_y^2 & u_x^2 & 4u_xu_y & 2u_y & 2u_x & 1 \end{bmatrix} \tag{53}$$

It may be noted that if $\mathbf{F}=\mathbf{F}(u_x,u_y)$, then $\mathbf{F}^{-1}=\mathbf{F}(-u_x,-u_y)$ (see Yahia and Premnath [65]).

Finally, we express the transformation matrix $\mathbf{P}^{-1}$ mapping a vector of (post-collision) raw moments $\tilde{\boldsymbol{\kappa}}'$ to a vector of (post-collision) distribution functions $\tilde{\mathbf{f}}$ as

$$\mathbf{P}^{-1}=\begin{bmatrix} 1 & 0 & 0 & -1 & -1 & 0 & 0 & 0 & 1\\ 0 & \frac{1}{2} & 0 & \frac{1}{2} & 0 & 0 & 0 & -\frac{1}{2} & -\frac{1}{2}\\ 0 & 0 & \frac{1}{2} & 0 & \frac{1}{2} & 0 & -\frac{1}{2} & 0 & -\frac{1}{2}\\ 0 & -\frac{1}{2} & 0 & \frac{1}{2} & 0 & 0 & 0 & \frac{1}{2} & -\frac{1}{2}\\ 0 & 0 & -\frac{1}{2} & 0 & \frac{1}{2} & 0 & \frac{1}{2} & 0 & -\frac{1}{2}\\ 0 & 0 & 0 & 0 & 0 & \frac{1}{4} & \frac{1}{4} & \frac{1}{4} & \frac{1}{4}\\ 0 & 0 & 0 & 0 & 0 & -\frac{1}{4} & \frac{1}{4} & -\frac{1}{4} & \frac{1}{4}\\ 0 & 0 & 0 & 0 & 0 & \frac{1}{4} & -\frac{1}{4} & -\frac{1}{4} & \frac{1}{4}\\ 0 & 0 & 0 & 0 & 0 & -\frac{1}{4} & -\frac{1}{4} & \frac{1}{4} & \frac{1}{4} \end{bmatrix} \tag{54}$$

Appendix C. Analytical solution of the energy equation: temperature field

The solution to the energy equation Eq. (10) is invariant with the nature of the fluid, i.e., whether it is for a NF or a SRF, and hence the results reported in Pendse and Esmaeeli [10] for the temperature field is valid here as well. However, for completeness, we provide all the necessary details involved in the solution procedure in what follows. The energy equation is homogeneous and has periodic boundary conditions in the x-direction. Furthermore, the only non-homogeneities are in the upper and lower boundary conditions. To solve this problem, the non-homogeneous boundary conditions can be split across two solutions as we will see next. The energy equation is given as in Eq. (10)

$$\frac{\partial^2 T}{\partial x^2}+\frac{\partial^2 T}{\partial y^2}=0, \tag{55}$$

which is subject to the following boundary conditions

$$T^b(x,-b)=T_h+\Delta T\cos(\omega x),$$

and

$$T^a(x,a)=T_c.$$

Because of the homogeneity and linearity of the differential equation and that the temperature is periodic in the horizontal direction, the method of separation of variables is used to solve the temperature equation,

$$T^i(x,y)=P^i(x,y)+Q^i(y), \qquad i=a,b, \tag{56}$$

where $P^i(x,y)$ and $Q^i(y)$ are the perturbation and linear temperature fields, respectively. Substituting Eq. (56) into the energy equation (Eq. (55)) gives the following separated equations that we need to solve

$$\frac{\partial^2 P^i}{\partial x^2}+\frac{\partial^2 P^i}{\partial y^2}=0, \qquad \text{and} \qquad \frac{\partial^2 Q^i}{\partial y^2}=0, \qquad i=a,b,$$

which are subject to the following boundary conditions.

i) The temperature is specified at the lower wall:

$$P^b(x,-b)=\Delta T\cos(\omega x), \qquad \text{and} \qquad Q^b(x,-b)=T_h.$$

ii) The temperature is specified at the upper wall:

$$P^a(x,a)=0, \qquad \text{and} \qquad Q^a(x,a)=T_c.$$

iii) The temperature is continuous at the interface:

$$P^a(x,0)=P^b(x,0), \qquad \text{and} \qquad Q^a(x,0)=Q^b(x,0).$$

iv) The heat flux is continuous at the interface:

$$-k_b\left.\frac{\partial P^b}{\partial y}\right|_{y=0}=-k_a\left.\frac{\partial P^a}{\partial y}\right|_{y=0},]$$

$$\text{and} \qquad -k_b\left.\frac{\partial Q^b}{\partial y}\right|_{y=0}=-k_a\left.\frac{\partial Q^a}{\partial y}\right|_{y=0}.$$

The solution for the linear temperature field is $Q^i(y)=A_1^iy+A_2^i$. Applying the above boundary conditions to get the constants of integration which yields in the solution for the lower wall

$$Q^b(y)=\frac{k_a(T_c-T_h)y+T_ck_ab+T_hk_ba}{(ak_b+bk_a)}. \tag{57}$$

Similarly, the solution for the upper wall is:

$$Q^a(y)=\frac{k_b(T_c-T_h)y+T_ck_ab+T_hk_ba}{(ak_b+bk_a)}. \tag{58}$$

Then by the standard separation of variables method, and by looking at the lower boundary condition, the solution for the perturbation in the temperature field $P^i(x,y)$ for the lower fluid is

$$P^b(x,y)=[A_1^b\cosh(\omega y)+A_2^b\sinh(\omega y)]\cos(\omega x). \tag{59}$$

Similarly, for the solution for the upper fluid is,

$$P^a(x,y)=[A_1^a\cosh(\omega y)+A_2^a\sinh(\omega y)]\cos(\omega x). \tag{60}$$

Now, by applying the above four boundary condition, we get the following constants

$$A_1^a=A_1^b=\Delta T\sinh(\tilde{a})f(\tilde{a},\tilde{b},\tilde{k}), \quad A_2^a=-\Delta T\cosh(\tilde{a})f(\tilde{a},\tilde{b},\tilde{k}),$$
$$A_2^b=-\Delta T\tilde{k}\cosh(\tilde{a})f(\tilde{a},\tilde{b},\tilde{k}),$$

where

$$f(\tilde{a},\tilde{b},\tilde{k})=\left[\tilde{k}\sinh(\tilde{b})\cosh(\tilde{a})+\sinh(\tilde{a})\cosh(\tilde{b})\right]^{-1}, \tag{61}$$

where $\tilde{a}=a\omega$, and $\tilde{b}=b\omega$, and $\tilde{k}=k_a/k_b$. Substitution of the above constants (A_1^a, A_2^a, A_1^b, and A_2^b) in Eqs. (59) and (60) results in the final solution of the perturbation temperature $P^i(x,y)$ in the lower fluid as

$$P^b(x,y)=\Delta T f(\tilde{a},\tilde{b},\tilde{k})[\sinh(\tilde{a})\cosh(\omega y)-\tilde{k}\sinh(\omega y)\cosh(\tilde{a})]\cos(\omega x). \tag{62}$$

Similarly, for the upper fluid,

$$P^a(x,y)=\Delta T f(\tilde{a},\tilde{b},\tilde{k})\sinh(\tilde{a}-\omega y)\cos(\omega x). \tag{63}$$

Appendix D. Characteristic thermocapillary velocity scale on the interface in self-rewetting fluids

The characteristic velocity scale can be derived by considering the balance of shear stress with the Marangoni stress due to the surface tension gradient on the interface. The shear stress scales as

$$\tau_\mu^b \sim \frac{\mu^b U_s}{b},$$

where b is the thickness of the lower fluid and U_s is the unknown characteristic velocity scale to be determined in what follows. Furthermore, the surface tension gradient scales as

$$\frac{d\sigma}{dx} \sim \frac{d\sigma}{dT}\frac{\Delta T}{l},$$

where l is the length of the microchannel, and for SRFs with a quadratic dependence of surface tension on temperature (see Eq. (4))

$$\frac{d\sigma}{dT} = \sigma_T + 2\sigma_{TT}\left(T - T_{ref}\right).$$

Thus, the velocity scale can be deduced by from the first two equations above by setting $\tau_\mu^b \sim d\sigma/dx$ and then substituting the last equation for $d\sigma/dT$ as

$$U_s \sim \frac{\Delta T}{\mu^b}\left(\frac{b}{l}\right)\frac{d\sigma}{dT} = \frac{\Delta T}{\mu^b}\left(\frac{b}{l}\right)\left[\sigma_T + 2\sigma_{TT}\left(T - T_{ref}\right)\right] \tag{64}$$

Here, we need a scale for the temperature on the interface, which we take it to be temperature field at $x = 0$ and $y = 0$, where it reaches a maximum. Now, using the temperature along the interface given as (see Appendix C)

$$T(x, y = 0) = C_1 + C_2\cos(\omega x),$$

and evaluating it at $x = 0$, we get

$$T(x = 0, y = 0) = C_1 + C_2, \tag{65}$$

where

$$C_1 = \frac{T_h\left(\frac{a}{b}\right) + T_c\tilde{k}}{\left(\frac{a}{b}\right) + \tilde{k}}, \quad C_2 = \frac{\Delta T\sinh(\tilde{a})}{\tilde{k}\cosh(\tilde{a})\sinh(\tilde{b}) + \cosh(\tilde{b})\sinh(\tilde{a})}, \tag{66}$$

Here, $\tilde{k} = k_a/k_b$, $\tilde{a} = a\omega$, and $\tilde{b} = b\omega$. Substituting the above estimate for the temperature scale on the interface in Eq. (64), we finally obtain the characteristic thermocapillary velocity scale in SRFs as

$$U_s \sim \frac{\Delta T}{\mu^b}\left(\frac{b}{l}\right)\left[\sigma_T + 2\sigma_{TT}\left(C_1 + C_2 - T_{ref}\right)\right]. \tag{67}$$

References

[1] P.-G. De Gennes, F. Brochard-Wyart, D. Quéré, et al., Capillarity and Wetting Phenomena: Drops, Bubbles, Pearls, Waves, vol. 315, Springer, 2004.

[2] L.E. Scriven, C.V. Sternling, The Marangoni effects, Nature 187 (4733) (1960) 186–188.

[3] R.F. Probstein, Physicochemical Hydrodynamics: An Introduction, John Wiley & Sons, 2005.

[4] N.O. Young, J.S. Goldstein, M.J. Block, The motion of bubbles in a vertical temperature gradient, J. Fluid Mech. 6 (3) (1959) 350–356.

[5] R.S. Subramanian, R. Balasubramaniam, N. Clark, Motion of bubbles and drops in reduced gravity, Appl. Mech. Rev. 55 (3) (2002) B56.

[6] S.W.J. Welch, Transient thermocapillary migration of deformable bubbles, J. Colloid Interface Sci. 208 (2) (1998) 500–508.

[7] C. Ma, D. Bothe, Direct numerical simulation of thermocapillary flow based on the volume of fluid method, Int. J. Multiph. Flow 37 (9) (2011) 1045–1058.

[8] A.A. Darhuber, S.M. Troian, Principles of microfluidic actuation by modulation of surface stresses, Annu. Rev. Fluid Mech. 37 (2005) 425–455.

[9] A. Karbalaei, R. Kumar, H.J. Cho, Thermocapillarity in microfluidics—A review, Micromachines 7 (1) (2016) 13.

[10] B. Pendse, A. Esmaeeli, An analytical solution for thermocapillary-driven convection of superimposed fluids at zero Reynolds and Marangoni numbers, Int. J. Therm. Sci. 49 (7) (2010) 1147–1155.

[11] T. Gambaryan-Roisman, Modulation of Marangoni convection in liquid films, Adv. Colloid Interface Sci. 222 (2015) 319–331.

[12] R. Vochten, G. Petre, Study of the heat of reversible adsorption at the air-solution interface. II. Experimental determination of the heat of reversible adsorption of some alcohols, J. Colloid Interface Sci. 42 (2) (1973) 320–327.

[13] G. Petre, M.A. Azouni, Experimental evidence for the minimum of surface tension with temperature at aqueous alcohol solution/air interfaces, J. Colloid Interface Sci. 98 (1) (1984) 261–263.

[14] M.C. Limbourg-Fontaine, G. Pétré, J.C. Legros, Thermocapillary movements under microgravity at a minimum of surface tension, Naturwissenschaften 73 (7) (1986) 360–362.

[15] D. Villers, J.K. Platten, Temperature dependence of the interfacial tension between water and long-chain alcohols, J. Phys. Chem. 92 (14) (1988) 4023–4024.

[16] Y. Abe, A. Iwasaki, K. Tanaka, Microgravity experiments on phase change of self-rewetting fluids, Ann. N. Y. Acad. Sci. 1027 (1) (2004) 269–285.

[17] Y. Abe, Terrestrial and microgravity applications of self-rewetting fluids, Microgravity Sci. Technol. 19 (3) (2007) 11–12.

[18] R. Savino, A. Cecere, R. Di Paola, Surface tension-driven flow in wickless heat pipes with self-rewetting fluids, Int. J. Heat Fluid Flow 30 (2) (2009) 380–388.

[19] R. Savino, A. Cecere, S. Van Vaerenbergh, Y. Abe, G. Pizzirusso, W. Tzevelecos, M. Mojahed, Q. Galand, Some experimental progresses in the study of self-rewetting fluids for the SELENE experiment to be carried in the thermal platform 1 hardware, Acta Astronaut. 89 (2013) 179–188.

[20] Y. Hu, T. Liu, X. Li, S. Wang, Heat transfer enhancement of micro oscillating heat pipes with self-rewetting fluid, Int. J. Heat Mass Transf. 70 (2014) 496–503.

[21] S.-C. Wu, T.-J. Lee, W.-J. Lin, Y.-M. Chen, Study of self-rewetting fluid applied to loop heat pipe with PTFE wick, Appl. Therm. Eng. 119 (2017) 622–628.

[22] A. Cecere, D. De Cristofaro, R. Savino, V. Ayel, T. Sole-Agostinelli, M. Marengo, C. Romestant, Y. Bertin, Experimental analysis of a flat plate pulsating heat pipe with self-rewetting fluids during a parabolic flight campaign, Acta Astronaut. 147 (2018) 454–461.

[23] M. Zhu, J. Huang, M. Song, Y. Hu, Thermal performance of a thin flat heat pipe with grooved porous structure, Appl. Therm. Eng. 173 (2020) 115215.

[24] A. Sitar, I. Golobic, Heat transfer enhancement of self-rewetting aqueous n-butanol solutions boiling in microchannels, Int. J. Heat Mass Transf. 81 (2015) 198–206.

[25] K. Sefiane, X. Yu, G. Duursma, J. Xu, On heat and mass transfer using evaporating self-rewetting mixtures in microchannels, Appl. Therm. Eng. 179 (2020) 115662.

[26] Y. Hu, S. Zhang, X. Li, S. Wang, Heat transfer enhancement of subcooled pool boiling with self-rewetting fluid, Int. J. Heat Mass Transf. 83 (2015) 64–68.

[27] Y. Hu, S. Chen, J. Huang, M. Song, Marangoni effect on pool boiling heat transfer enhancement of self-rewetting fluid, Int. J. Heat Mass Transf. 127 (2018) 1263–1270.

[28] Y. Hu, H. Wang, M. Song, J. Huang, Marangoni effect on microbubbles emission boiling generation during pool boiling of self-rewetting fluid, Int. J. Heat Mass Transf. 134 (2019) 10–16.

[29] Y.I. Kim, B.-H. Bang, K. Jang, S. An, A.L. Yarin, S.S. Yoon, Pool boiling enhancement via nanotexturing and self-propelled swing motion for bubble shedding, Int. Commun. Heat Mass Transf. 133 (2022) 105934.

[30] I. Zaaroura, S. Harmand, J. Carlier, M. Toubal, A. Fasquelle, B. Nongaillard, Thermal performance of self-rewetting gold nanofluids: application to two-phase heat transfer devices, Int. J. Heat Mass Transf. 174 (2021) 121322.

[31] M.E.R. Shanahan, K. Sefiane, Recalcitrant bubbles, Sci. Rep. 4 (1) (2014) 1–9.

[32] D. Mamalis, V. Koutsos, K. Sefiane, Bubble rise in a non-isothermal self-rewetting fluid and the role of thermocapillarity, Int. J. Therm. Sci. 117 (2017) 146–162.

[33] Y. Hu, K. Huang, J. Huang, A review of boiling heat transfer and heat pipes behaviour with self-rewetting fluids, Int. J. Heat Mass Transf. 121 (2018) 107–118.

[34] A. Oron, P. Rosenau, On a nonlinear thermocapillary effect in thin liquid layers, J. Fluid Mech. 273 (1994) 361–374.

[35] W. Batson, Y. Agnon, A. Oron, Thermocapillary modulation of self-rewetting films, J. Fluid Mech. 819 (2017) 562–591.

[36] Z. Yu, Thermocapillary instability of self-rewetting films on vertical fibers, Phys. Fluids 30 (8) (2018) 082104.

[37] S.G. Slavtchev, S.P. Miladinova, Thermocapillary flow in a liquid layer at minimum in surface tension, Acta Mech. 127 (1) (1998) 209–224.

[38] M.K. Tripathi, K.C. Sahu, G. Karapetsas, K. Sefiane, O.K. Matar, Non-isothermal bubble rise: non-monotonic dependence of surface tension on temperature, J. Fluid Mech. 763 (2015) 82–108.

[39] B.R. Duffy, S.K. Wilson, J. Conn, K. Sefiane, Unsteady motion of a long bubble or droplet in a self-rewetting system, Phys. Rev. Fluids 3 (12) (2018) 123603.

[40] M. Balla, M.K. Tripathi, K.C. Sahu, G. Karapetsas, O.K. Matar, Non-isothermal bubble rise dynamics in a self-rewetting fluid: three-dimensional effects, J. Fluid Mech. 858 (2019) 689–713.

[41] M. Majidi, R. Haghani-Hassan-Abadi, M.-H. Rahimian, Single recalcitrant bubble simulation using a hybrid lattice Boltzmann finite difference model, Int. J. Multiph. Flow 127 (2020) 103289.

[42] T.R. Mitchell, M. Majidi, M.H. Rahimian, C.R. Leonardi, Computational modeling of three-dimensional thermocapillary flow of recalcitrant bubbles using a coupled lattice Boltzmann-finite difference method, Phys. Fluids 33 (3) (2021) 032108.

[43] R. Benzi, S. Succi, M. Vergassola, The lattice Boltzmann equation: theory and applications, Phys. Rep. 222 (3) (1992) 145–197.

[44] D. Yu, R. Mei, L.-S. Luo, W. Shyy, Viscous flow computations with the method of lattice Boltzmann equation, Prog. Aerosp. Sci. 39 (5) (2003) 329–367.

[45] P. Lallemand, L.-s. Luo, M. Krafczyk, W.-A. Yong, The lattice Boltzmann method for nearly incompressible flows, J. Comput. Phys. 431 (2021) 109713.

[46] X. He, S. Chen, R. Zhang, A lattice Boltzmann scheme for incompressible multiphase flow and its application in simulation of Rayleigh–Taylor instability, J. Comput. Phys. 152 (2) (1999) 642–663.

[47] X. He, G.D. Doolen, Thermodynamic foundations of kinetic theory and lattice Boltzmann models for multiphase flows, J. Stat. Phys. 107 (1) (2002) 309–328.

[48] T. Lee, C.-L. Lin, A stable discretization of the lattice Boltzmann equation for simulation of incompressible two-phase flows at high density ratio, J. Comput. Phys. 206 (1) (2005) 16–47.

[49] K.N. Premnath, J. Abraham, Three-dimensional multi-relaxation time (MRT) lattice-Boltzmann models for multiphase flow, J. Comput. Phys. 224 (2) (2007) 539–559.

[50] F. Hajabdollahi, K.N. Premnath, S.W.J. Welch, Central moment lattice Boltzmann method using a pressure-based formulation for multiphase flows at high density ratios and including effects of surface tension and Marangoni stresses, J. Comput. Phys. 425 (2021) 109893.

[51] H. Liu, Y. Zhang, A.J. Valocchi, Modeling and simulation of thermocapillary flows using lattice Boltzmann method, J. Comput. Phys. 231 (12) (2012) 4433–4453.

[52] M. Geier, A. Greiner, J.G. Korvink, Cascaded digital lattice Boltzmann automata for high Reynolds number flow, Phys. Rev. E 73 (6) (2006) 066705.

[53] W.E. Langlois, M.O. Deville, Slow Viscous Flow, vol. 173436, Springer, 2014.

[54] P.-H. Chiu, Y.-T. Lin, A conservative phase field method for solving incompressible two-phase flows, J. Comput. Phys. 230 (1) (2011) 185–204.

[55] Y. Sun, C. Beckermann, Sharp interface tracking using the phase-field equation, J. Comput. Phys. 220 (2) (2007) 626–653.

[56] R. Folch, J. Casademunt, A. Hernández-Machado, L. Ramirez-Piscina, Phase-field model for hele-shaw flows with arbitrary viscosity contrast. I. Theoretical approach, Phys. Rev. E 60 (2) (1999) 1724.

[57] J.U. Brackbill, D.B. Kothe, C. Zemach, A continuum method for modeling surface tension, J. Comput. Phys. 100 (2) (1992) 335–354.

[58] A. Kumar, Isotropic finite-differences, J. Comput. Phys. 201 (1) (2004) 109–118.

[59] H. Ding, P.D.M. Spelt, C. Shu, Diffuse interface model for incompressible two-phase flows with large density ratios, J. Comput. Phys. 226 (2) (2007) 2078–2095.

[60] T. Krüger, H. Kusumaatmaja, A. Kuzmin, O. Shardt, G. Silva, E.M. Viggen, The lattice Boltzmann method, Springer Int. Publ. 10 (978-3) (2017) 4–15.

[61] Z. Guo, P. Lin, A thermodynamically consistent phase-field model for two-phase flows with thermocapillary effects, J. Fluid Mech. 766 (2015) 226–271.

[62] L. Zheng, S. Zheng, Q. Zhai, Continuous surface force based lattice Boltzmann equation method for simulating thermocapillary flow, Phys. Lett. A 380 (4) (2016) 596–603.

[63] S.A. Nabavizadeh, M. Eshraghi, S.D. Felicelli, S.N. Tewari, R.N. Grugel, Effect of bubble-induced Marangoni convection on dendritic solidification, Int. J. Multiph. Flow 116 (2019) 137–152.

[64] K.N. Premnath, S. Banerjee, Incorporating forcing terms in cascaded lattice Boltzmann approach by method of central moments, Phys. Rev. E 80 (3) (2009) 036702.

[65] E. Yahia, K.N. Premnath, Central moment lattice Boltzmann method on a rectangular lattice, Phys. Fluids 33 (5) (2021) 057110.

[66] E. Yahia, W. Schupbach, K.N. Premnath, Three-dimensional central moment lattice Boltzmann method on a cuboid lattice for anisotropic and inhomogeneous flows, Fluids 6 (9) (2021) 326.

[67] M. Geier, M. Schönherr, A. Pasquali, M. Krafczyk, The cumulant lattice Boltzmann equation in three dimensions: theory and validation, Comput. Math. Appl. 70 (4) (2015) 507–547.